JACS Au
AN OPEN ACCESS JOURNAL OF THE AMERICAN CHEMICAL SOCIETY

pubs.acs.org/jacsau
Article

Competition between Mononuclear and Binuclear Copper Sites across Different Zeolite Topologies

Asanka Wijerathne, Allison Sawyer, Rohil Daya, and Christopher Paolucci*

Cite This: JACS Au 2024, 4, 197−215
Read Online

ACCESS | Metrics & More | Article Recommendations | Supporting Information

ABSTRACT: A key challenge for metal-exchanged zeolites is the determination of metal cation speciation and nuclearity under synthesis and reaction conditions. Copper-exchanged zeolites, which are widely used in automotive emissions control and potential catalysts for partial methane oxidation, have in particular evidenced a wide variety of Cu structures that are observed to change with exposure conditions, zeolite composition, and topology. Here, we develop predictive models for Cu cation speciation and nuclearity in CHA, MOR, BEA, AFX, and FER zeolite topologies using interatomic potentials, quantum chemical calculations, and Monte Carlo simulations to interrogate this vast configurational and compositional space. Model predictions are used to rationalize experimentally observed differences between Cu-zeolites in a wide-body of literature, including nuclearity populations, structural variations, and methanol per Cu yields. Our results show that both topological features and commonly observed Al-siting biases in MOR zeolites increase the population of binuclear Cu sites, explaining the small population of mononuclear Cu sites observed in these materials relative to other zeolites such as CHA and BEA. Finally, we used a machine learning classification model to determine the preference to form mononuclear or binuclear Cu sites at different Al configurations in 200 zeolites in the international zeolite database. Model results reveal several zeolite topologies at extreme ends of the mononuclear vs binuclear spectrum, highlighting synthetic options for realization of zeolites with strong Cu nuclearity preferences.

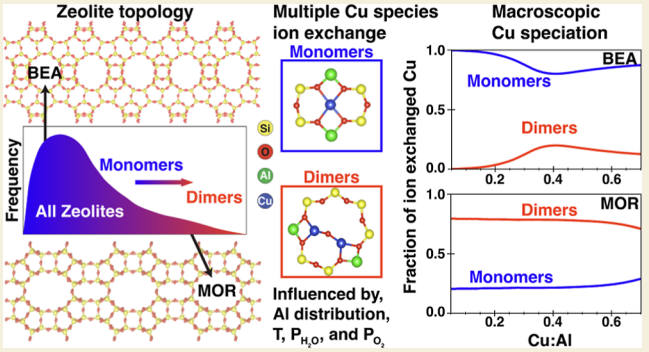

KEYWORDS: *catalysts, cations, zeolites, hydrocarbons, metal clusters*

INTRODUCTION

Active site heterogeneity is a key concept in heterogeneous catalysis and a primary challenge is identifying active sites and their distribution.[1−4] Active site heterogeneity can stem from differences in ligands and atomic environments,[1,5−7] including variations in the nuclearity of metal active sites.[8−11] Materials containing a distribution of metal active site nuclearities can show drastic differences in reactivity for reactions including ethylene hydrogenation,[12−14] D_2 exchange in CH_4,[15] and partial methane oxidation (PMO).[8,16−22] Copper-exchanged zeolites in particular have shown sensitivity to active site nuclearity for a number of reactions including the selective catalytic reduction (SCR) of NO_x[4,23,24] catalytic or stepwise PMO,[16,18,20] and NO oxidation.[25] Here, we develop condition-dependent computational models for Cu speciation in a wide variety of zeolite topologies and compositions. We use our models to rationalize reported trends and observations in a wide body of experimental literature and determine specific zeolite topologies that favor the formation of either mononuclear or binuclear Cu complexes.

The nuclearity of ion-exchanged Cu is sensitive to structural and compositional features of the zeolite host. Zeolites are nanoporous aluminosilicates consisting of TO_4 tetrahedral primary building units (T = Si or Al), which connect to form different size rings and cages known as secondary building units (SBUs) that comprise different 3D crystalline zeolite topologies (Figure 1). Substitution of Al in the zeolite lattice creates anionic sites ($[AlO_2]^-$) that are charge compensated by extra framework cations. The speciation of those cations is dictated by the arrangement of anionic Al configurations[26−30] and exposure conditions.[29−32] For example, in the presence of H_2O at low (<473 K) temperatures, these cations form solvated complexes detached from the zeolite framework, such as $[Cu(H_2O)_4]^{2+}$, and are less sensitive to specific Al arrangements and zeolite topologies.[31,33,34] However, at higher temperatures, Cu ions bond to the zeolite framework and form structures such as $Z_2^{2-}Cu^{2+}$ or Z^-Cu^+, where Z denotes an

Received: October 18, 2023
Revised: December 12, 2023
Accepted: December 20, 2023
Published: January 4, 2024

https://doi.org/10.1021/jacsau.3c00632
JACS Au 2024, 4, 197−215

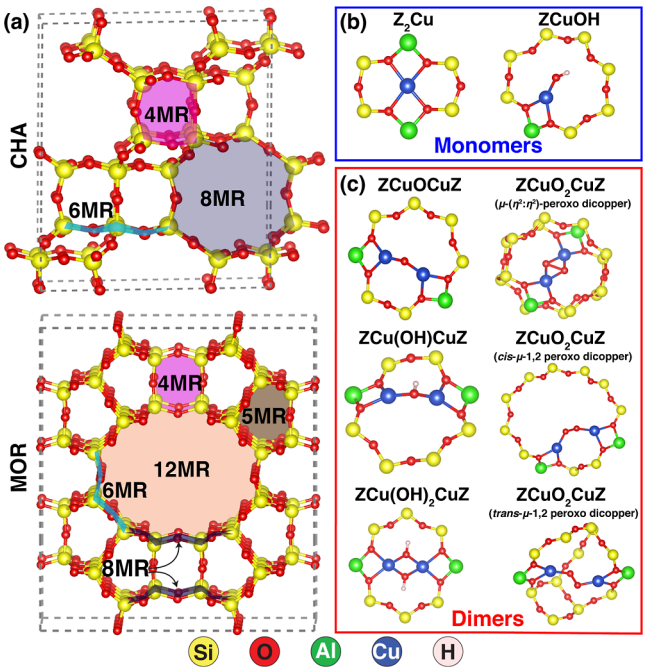

Figure 1. Different ring structures and extra framework Cu species present in zeolites (a) CHA framework (top) and MOR framework (bottom), (b) Cu-monomer species, (c) Cu-dimer species.

anionic charge ($[AlO_2]^-$) in the zeolite framework.[4,31,35] The parent zeolite's Al distribution is mainly determined by the synthesis conditions,[28,36,37] although postsynthesis protocols such as hydrothermal aging and dealumination can alter the Al distribution.[38−40] However, once the parent zeolite is synthesized with charge-compensating cations such as Na^+, H^+, or NH_4^+, literature evidence suggests[1,3,23,41] that the thermodynamics of Cu cation exchange largely dictates the formation of different Cu sites because framework Al is relatively immobile under typical ion exchange conditions.[41−43]

The nuclearity and ligand environment of Cu sites depend on exposure conditions, Al distribution, and zeolite topology.[1,4,23,32,44−46] Figure 1a shows CHA and MOR, two zeolites that are topologically different (other zeolite topologies are discussed below). We hypothesized that these topological differences may result in variation of Cu speciation, even at similar compositions (Si/Al and Cu/Al). For example, Z_2Cu monomers (Figure 1b) preferentially occupy 2Al configurations in six-membered rings (6MR) in CHA[27,31,47,48] and other zeolites,[36,49] while 8MRs in CHA, MOR, and other zeolites such as MFI and MAZ, appear to demonstrate a preference for multinuclear Cu species (Figure 1c).[18,32] Isolated Z_2Cu sites have been shown to be inactive for PMO reactions,[18,50,51] whereas multinuclear Cu species,[18,52−55] or proximal mononuclear Cu species,[56] are suggested as active sites. Although the exact nature of Cu active sites for PMO is debated, various forms of multinuclear Cu sites, and Cu dimers most commonly, have been implicated as active sites.[8,18,32,52,53,57] The abundance of multinuclear Cu species in zeolites such as MOR could in part explain their higher methanol yields (per Cu) compared to other zeolites such as CHA,[18,52] where redox-resistant isolated Z_2Cu species may inhibit PMO reactivity. Similarly, for high temperature (>523 K) SCR and oxidation of NO or NH_3,[11,25,58,59] framework-coordinated Cu dimers in CHA have been implicated as active sites, and their number and speciation may impact high temperature performance when comparing zeolites with different Al distributions and topologies. While these observations support zeolite composition and topology as important factors in Cu speciation, many unknowns remain. Why does MOR appear to have a higher population of multinuclear Cu species than CHA at most compositions? More broadly, why (at equivalent exposure conditions) do certain Al distributions and zeolite topologies show a preference for forming Cu monomers or dimers, and can this preference be predicted?

Here, we use a combination of machine learning-based interatomic potentials, DFT calculations, and Monte Carlo simulations, to estimate the relative populations of different Cu species across a wide variety of zeolite topologies. We show that the nuclearity of Cu species depends sensitively on temperature and the availability of specific 2Al configurations, and the multiplicity of these configurations is zeolite topology-dependent. Our results rationalize experimentally observed differences in PMO performance between different zeolites, and experimentally quantified variations in Cu dimer populations as a function of temperature and topology. Finally, we show that a machine learning-based classification model, using geometry and void space descriptors, is capable of discriminating the propensity to form mononuclear or binuclear Cu sites at specific 2Al configurations in zeolite topologies across the international zeolite database (IZDB).

RESULTS AND DISCUSSION

Al Configuration-Dependent Free Energies of Cu Motifs

Extra framework Cu cations charge-compensated by zeolite framework Al (Z) can form either mononuclear or multinuclear complexes. The type of complex formed is dictated by the sample history and external conditions (temperature and pressures), the macroscopic composition of the zeolite (Si/Al and Cu/Al), and at a given composition, the distribution of Al arrangements. Ensembles of multiple Al result in a distribution of environments for cation siting. To make the resulting configurational space tractable, we limit our analysis to 1Al and 2Al configurations, oxidizing hydrothermal conditions (O- and H-containing Cu motifs) relevant to chemistries such as PMO and high-temperature SCR, and monomer and dimer Cu nuclearities. To determine the relative likelihood for different Cu species to form in a variety of zeolite topologies (vide infra), we computed Cu exchange free energies (all energies were computed using DFT, see Methods and Section S5 for free energy approximations) at each symmetry distinct 1Al, and 2Al configuration within an Al−Al separation distance of 10 Å. At distances longer than 10 Å, both Al are treated as functionally isolated 1Al sites and are assumed to exchange only ZCuOH (see Methods). For each 2Al configuration, the computed Cu motifs (Figure 1b,c) included monomers: Z_2Cu and 2ZCuOH, and dimers: Z_2Cu_2O, $Z_2Cu_2O_2$ (trans, cis, and η^2: η^2 isomers), Z_2Cu_2OH, and $Z_2Cu_2(OH)_2$. These species were selected because they are the most thermodynamically stable Cu^{2+} motifs reported in previous experimental and computational studies over a wide range of oxidizing conditions,[17,31,32,35,48,60−65] although under some oxidizing conditions, a minority fraction of these species may "autoreduce" to ZCu (vide infra). For a given Cu motif and Al configuration, the free energy to exchange Cu for the Brønsted acid sites in the proton form zeolite can be computed

https://doi.org/10.1021/jacsau.3c00632
JACS Au 2024, 4, 197−215

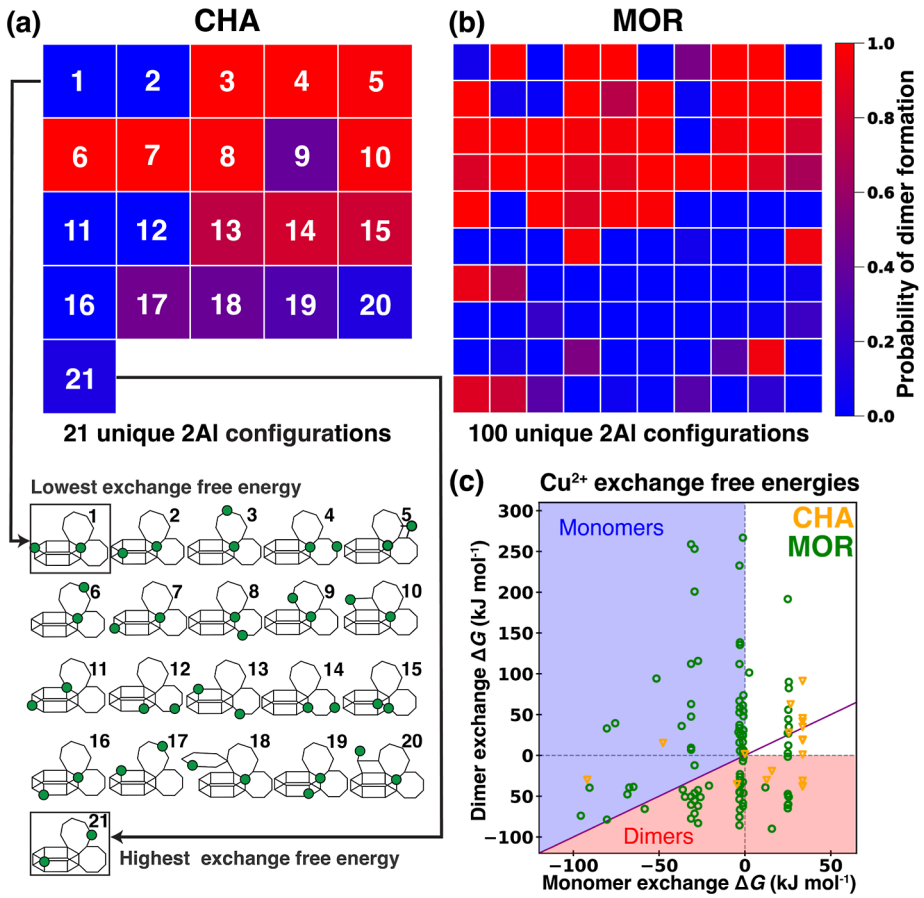

Figure 2. Probability of dimer formation computed by eq 5 at 10^{-6} kPa H_2O, 20 kPa O_2, 973 K, for the (a) 21 symmetrically unique 2Al configurations in CHA and the (b) 100 symmetrically unique 2Al configurations in MOR. Each square in the upper two panels represents symmetrically unique 2Al configurations in ascending exchange free energy order as numbered in the upper left panel. Schematics of respective 2Al configurations for CHA are shown in the (a) lower panel. (c) The lowest Cu^{2+} exchange free energies of monomers and dimers computed using eq 1 for each 2Al configuration within an Al−Al distance of 10 Å. The marks that form linear columns with roughly constant monomer exchange free energies are 2Al configurations that have 2ZCuOH (Figure S4.3) as the most stable monomer.

for a set of gas conditions (T, P_{H_2O}, P_{O_2}) and relative to a Cu reference state. We chose CuO(s) as a convenient reference state, which results in the following general equation for cation exchange

$$Z_2H_2(s) + xCuO(s) + \frac{(2y - 2x - z + 2)}{4}O_2(g) + \frac{(z-2)}{2}H_2O(g) \xrightarrow{\Delta G_{species}} Z_2Cu_xO_yH_z(s) \quad (1)$$

For example, this equation reduces to the following for three of the possible Cu motifs

$$Z_2H_2 + CuO \xrightarrow{\Delta G_{Z_2Cu}} Z_2Cu + H_2O \quad (2)$$

$$Z_2H_2 + 2CuO \xrightarrow{\Delta G_{Z_2Cu_2O}} Z_2Cu_2O + H_2O \quad (3)$$

$$Z_2H_2 + 2CuO \xrightarrow{\Delta G_{2ZCuOH}} 2ZCuOH \quad (4)$$

DFT energies were computed for all Z_2H_2 structures with different 2Al configurations, and details of the free energy calculations, structure generation, and sequential optimizations for all Cu-containing structures are reported in Methods section and Sections S2 and S4. The result of these calculations is an exchange free energy for each of the six Cu motifs at each 2Al configuration (e.g., the 21 2Al configurations in CHA that obey Löwenstein's rule, Figure 2a, result in 126 computed free energies).

To evaluate the probability of forming a certain Cu species (s) relative to others at a given aluminum configuration (i), we used the relative exchange free energies ($\Delta G_{i,s}$) for each species and assumed they follow a Boltzmann distribution and are kinetically accessible. Therefore, the probability ($p_{i,s}$) for species s to form at 2Al site i is

$$p_{i,s} = \frac{\exp\left(\frac{-\Delta G_{i,s}}{RT}\right)}{\sum_s^{\text{All Cu species}} \exp\left(\frac{-\Delta G_{i,s}}{RT}\right)} \quad (5)$$

This approach does not assume any Al distribution and gives Cu speciation probabilities for all 2Al configurations in each zeolite. To begin, we chose CHA and MOR (other zeolite topologies are discussed later) due to their topological differences (Figure 1a) and because previous studies have shown that Cu-dimers are the majority Cu motif in MOR at a wide range compositions,[8,66−68] whereas prior experimental and computational results show Cu preferentially occupies the 6MR in CHA forming Z_2Cu monomers.[27,31,47,48,69,70]

Figure 2a,b reports the Cu speciation predictions for each distinct 2Al configuration in CHA and MOR, respectively, at

https://doi.org/10.1021/jacsau.3c00632
JACS Au 2024, 4, 197−215

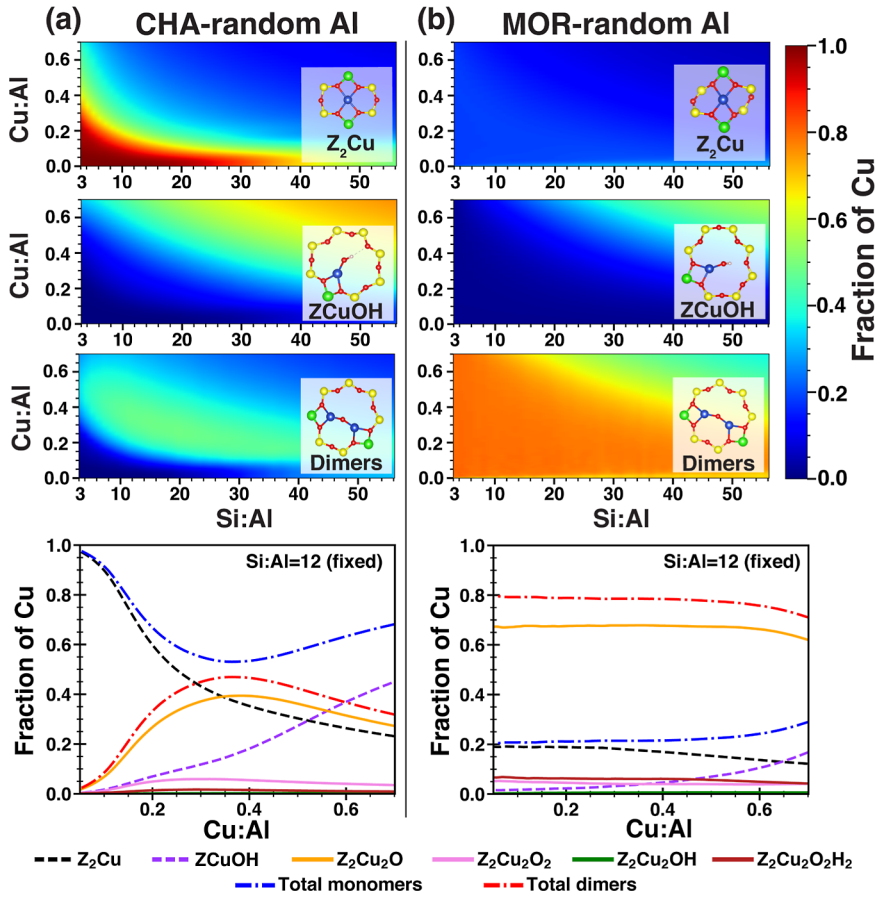

Figure 3. Predicted Cu speciation for a random Al distribution at conditions of 10^{-6} kPa H_2O, 20 kPa O_2 at 973 K (a) in CHA zeolite and (b) in MOR zeolite as a function of material composition (Si/Al and Cu/Al). The Cu dimer heatmaps report the summation of all types of dimers, as shown in Figure 1c. The population of all Cu species in Cu-CHA and Cu-MOR with fixed Si/Al = 12 as a function of Cu/Al is shown in the bottom panels.

973 K, 10^{-6} kPa H_2O, and 20 kPa O_2. This condition is representative of a high-temperature oxidative treatment in dry air and yields analogous results to 773 K at 10^{-8} kPa H_2O and 20 kPa O_2 (other conditions at lower temperatures and variable H_2O kPa are explored below and in Section S6). For ease of visualization, the summed probabilities for both monomers are compared to the summed probabilities of the four dimers, and the most exergonic monomer and dimer exchange energy for each 2Al configuration is reported in Figure 2c. Each square in the grid represents a 2Al configuration, and all 2Al configurations are treated as equally likely here. The squares are ordered in ascending order of Cu exchange free energies (using the most exergonic exchange energy among all Cu species) from left to right, and top to bottom, as numbered in Figure 2a upper panel, placing the most thermodynamically preferred exchange reaction among all 2Al configurations in the top-left corner and the least favorable in the bottom-right corner. The equilibrium populations of Cu monomers and dimers will depend on both the relative exchange energies and the abundance of specific 2Al exchange configurations, which is explored in the next section. For CHA, the 3NN-6MR configuration has the lowest Cu exchange free energy (Figure 2a, lower panel) followed by the 2NN-6MR configuration, and both configurations exchange Cu as Z_2Cu monomers consistent with prior studies.[27,31,70,71] Similarly, in MOR, the lowest Cu exchange free energy occurs at a 2Al site in a 3NN-6MR configuration located in the side pockets of MOR (Figure 1a) and exchanges Cu as a Z_2Cu monomer (Figure 2b). In both zeolites, the lowest free energy Cu dimers are predominately located at 8MR 2Al sites, and dimers form only up to 2Al separation distances of 8.2 and 9.4 Å, in CHA and MOR, respectively (Figure S5.1). These results show that both CHA and MOR have several 2Al exchange sites that preferentially exchange either monomers or dimers; rationalizing the observed differences in Cu speciation between the two zeolites requires knowledge of the 2Al configuration multiplicities and the Al distribution.

Figure 2c shows the most exergonic exchange energy for a monomer and dimer at each 2Al configuration in CHA and MOR. The competition between dimer and monomer formation at each 2Al configuration (i) is dictated by these relative exchange energies, as indicated by the blue and red shaded regimes separated by the purple line ($\Delta G_{i,\mathrm{monomer}} = \Delta G_{i,\mathrm{dimer}}$) in Figure 2c. For example, if the monomer exchange free energy is less than the dimer exchange free energy ($\Delta G_{i,\mathrm{monomer}} < \Delta G_{i,\mathrm{dimer}}$), that 2Al configuration thermodynamically favors Cu monomer exchange, and vice versa. The upper right quadrant shows configurations that exchange Cu endergonically at these conditions, which for CHA consists of 7 2Al configurations (7-2ZCuOH), and for MOR 11 configurations (11-2ZCuOH). Thermodynamically, Cu speciation will be biased toward more exergonic 2Al exchange

https://doi.org/10.1021/jacsau.3c00632
JACS Au 2024, 4, 197−215

configurations and corresponding species for a given zeolite, provided that each 2Al configuration is available in the zeolite.

Cu Speciation as a Function of Zeolite Composition

To assess equilibrium macroscopic Cu speciation as a function of Si/Al and Cu/Al in CHA and MOR zeolites at 973 K, 10^{-6} kPa H_2O and 20 kPa O_2, we used Monte Carlo (MC) simulations[31,72−75] as detailed in Methods. In brief, using an ensemble of large zeolite supercells, we titrate 2Al sites with Cu motifs according to the computed Cu exchange free energy probabilities (eq 19, more exergonic exchange free energies correspond to higher probabilities) and record the identities of the Cu species and the 2Al configurations they populate. The aluminum distribution of a zeolite depends on the synthesis protocol[28,76,77] and postsynthetic modifications.[37−40,78−80] We initially assumed a pseudorandom aluminum distribution (referred to as random Al) in our MC simulations; other Al distributions are explored further below. We excluded the 1NN 2Al configurations when populating Al because such 2Al pairs are unlikely to form in synthetic zeolites according to Löwenstein's rule.[81]

Figure 3 reports the computed fraction of Cu corresponding to each species (divided by total Cu) for varying Cu/Al and Si/Al compositions. In CHA (Figure 3a), Z_2Cu monomers are the majority species at low Cu loading and Al rich compositions, consistent with ca. zero Cu dimer formation probabilities at these sites for CHA (Figure 2a). However, the fraction of Z_2Cu monomers decreases as Cu/Al and Si/Al ratios increase in CHA, due to saturation of the available 6MR 2Al sites. The Cu/Al and Si/Al values that 6MR 2Al sites saturate with Z_2Cu at are identical to previous studies.[31,75] With increasing Cu loading, the fraction of Cu dimers increases, with a maximum population of Cu dimers (0.49) reached at Si/Al = 21 and Cu/Al = 0.26. This saturation phenomena is similar to Cu-exchange of zeolite-Y,[82] where Cu is first exchanged as Cu^{2+} monomers at proximal 2Al sites and at increasing Cu loading forms primarily $[Cu−O−Cu]^{2+}$ dimers separated by longer Al−Al distances. Conversely, in MOR, the majority Cu species are dimers (Figure 3b) and the total fraction of Cu dimers is close to constant over a wide range of Cu loadings (Cu/Al < 0.6) and Si/Al ratios (Si/Al < 40). For a given Si/Al, the saturation of Z_2Cu in CHA (Figure 3a) indicates that the Z_2Cu population is limited by the availability of 6MR 2Al exchange sites (2Al configurations 1 and 2 in Figure 2a) in a random Al distribution, whereas the constant dimer fraction in MOR indicates the abundance of 2Al sites in a random Al distribution that preferentially exchange Cu as dimers. Nevertheless, at the highest Si/Al and Cu/Al (upper right corner of the heatmaps), ZCuOH monomers are the majority species in both zeolites, due to the low number of Al per unit cell, statistically limiting (for a random Al distribution) the formation of 2Al sites within 10 Å, which are required to form either Z_2Cu monomers or Cu dimers as detailed in Section S5.3.

The fraction of Cu dimers depends on the zeolite topology; for all compositions, the fraction of Cu dimers is higher in MOR than in CHA (Figure 3a,b). This difference stems from MOR facilitating dimer formation even at low Cu/Al, whereas in CHA, Cu dimers populate only after a threshold Cu loading (that increases with decreasing Si/Al) is achieved due to saturation of 6MR 2Al configurations. In MOR, despite the lowest exchange free energy 2Al configuration forming Z_2Cu monomers, a Cu/Al threshold for dimer formation does not exist because the lowest energy Cu-exchange 2Al configuration (upper-left square in Figure 2b) has a lower statistical probability of occurrence than other 2Al configurations that form dimers with slightly higher exchange energy (+5 to 20 kJ mol^{-1}, see Figure S7.1b) due to differences in the multiplicities of the four symmetry distinct T-sites in MOR.

At high temperature and dry conditions (973 K, 10^{-6} kPa H_2O and 20 kPa O_2), Z_2Cu_2O accounts for >90% of all dimers across a wide range of compositions in both CHA and MOR zeolites (Figure 3-bottom). Consequently, independent MC simulations at these conditions with only Z_2Cu, ZCuOH, and Z_2Cu_2O species show only a small decrease (≈5%) in the total dimer population (Section S6.6). These results suggest that Z_2Cu_2O is a reasonable computational probe for estimating the equilibrium total dimer fraction at high temperature dry conditions. Moreover, previous experimental studies have shown spectroscopic evidence for Z_2Cu_2O as the majority Cu dimer site in Cu-MOR,[61,66,68,83] Cu-MFI,[53,84,85] and zeolite-Y[86] following exposure to high temperature dry air treatments. Therefore, for the next set of widely used zeolites we studied, BEA, AFX, and FER, we used computed free energies for only Z_2Cu, ZCuOH, and Z_2Cu_2O species.

Figure S6.2 shows the dimer formation probabilities for BEA, FER, and AFX. The AFX zeolite has a probability map similar to CHA, where the lowest energy Cu exchange 2Al sites are Z_2Cu monomers, followed by dimers and ZCuOH. Consequently, the MC-generated composition diagrams for AFX, shown in Figure S6.3b, are very similar to that of CHA, which is unsurprising because CHA and AFX have similar ring sizes, the same SBUs, and share the same double six-membered ring composite building unit, although the connectivity and the cage sizes are different.[87] Zeolite BEA, a large pore zeolite with 12−6−5−4 rings, has a much lower percentage of 2Al sites that preferentially form dimers (Figures S6.2c and S6.3a) compared to CHA, MOR, and AFX zeolites at similar conditions. FER and MOR have different ring topologies, yet MC simulations reveal that the Cu speciation in both zeolites show no threshold Cu/Al required to form dimers despite Z_2Cu monomers being the most exergonic Cu species in both zeolite topologies. Lack of a Cu/Al threshold for dimer formation indicates that, for a random Al distribution, 2Al sites that preferentially exchange Cu^{2+} dimers are abundant in both zeolites (Section S7). However, more ZCuOH form in FER (Figure S6.3c) than in MOR at similar compositions and conditions. Although these MC simulations with random Al distributions serve as a useful benchmark, both synthetic Al distributions (discussed below) and kinetic limitations for reaching equilibrium Cu dimer populations will play a role in determining Cu speciation.

Temperature Effects on Cu Speciation

Figure 4 reports the temperature-dependent Cu speciation (from MC simulations at different temperatures) for CHA and MOR at fixed compositions (Si/Al = 12 and Cu/Al = 0.4, 2.1 wt % Cu) representative of commonly reported synthetic zeolites.[18,80,88,89] The Z_2Cu fraction is roughly constant across different temperatures in both zeolites. At temperatures below 700 K, the majority of dimers are $Z_2Cu_2(OH)_2$. As temperature rises from 600 to 1000 K, the $Z_2Cu_2(OH)_2$ and ZCuOH populations decrease, and the Z_2Cu_2O population increases. The increasing population of Z_2Cu_2O is entropically driven through liberation of water by the reactions

$$Z_2Cu_2(OH)_2 \rightleftharpoons Z_2Cu_2O + H_2O \quad (6)$$

https://doi.org/10.1021/jacsau.3c00632
JACS Au 2024, 4, 197−215

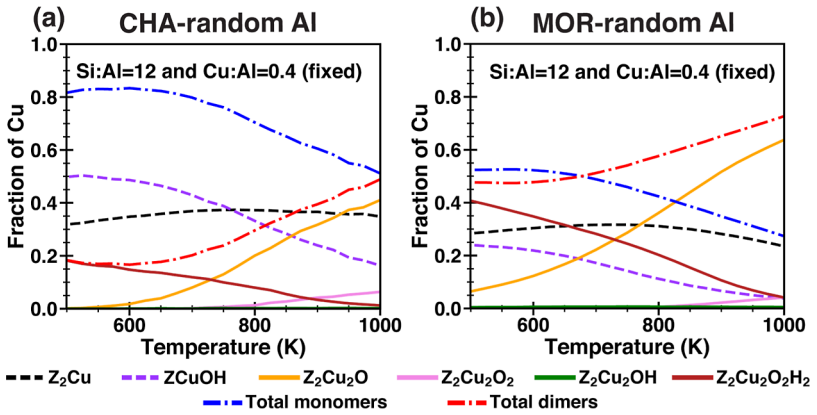

Figure 4. Temperature dependence of Cu speciation at 10^{-6} kPa H_2O, 20 kPa O_2 for a random Al distribution in (a) CHA and (b) MOR. Compositions for simulations were fixed at Si/Al = 12 and Cu/Al = 0.4 for both zeolites.

and

$$2ZCuOH \rightleftharpoons Z_2Cu_2O + H_2O \quad (7)$$

Consistent with this role of H_2O, Figure S6.6 shows that the temperature where $Z_2Cu_2(OH)_2$ and 2ZCuOH transition to Z_2Cu_2O depends sensitively on H_2O pressure. Lower H_2O pressures (10^{-7} to 10^{-8} kPa H_2O) promote formation of Z_2Cu_2O at lower temperatures. Only ZCuOH pairs charge-compensating 2Al within a maximum separation of 8.2 Å (CHA) and 9.4 Å (MOR) of each other (Section S5.3) convert to Z_2Cu_2O with increasing temperature; further than these distances, 2ZCuOH remain lower in free energy than possible dimers.

Spectroscopic and kinetic experiments have suggested that 2ZCuOH monomers may convert to Cu dimers[33,44,48,58,63,68,90−92] under a variety of reaction conditions. Pappas et al.[50] observed a decrease in νCuOH (ca. 3650 cm^{-1}) using in situ FT-IR, and a concomitant increase in Raman features assigned to Z_2Cu_2O from 523 to 673 K in their CHA materials. Similar observations and proposals of monomeric sites converting to dimers have been invoked for MOR using XANES,[61] CO-TPR,[68] electron paramagnetic resonance, operando UV−vis, in situ photoluminescence, and FT-IR.[56] Moreover, the proximity of ZCuOH sites, altered by varying Si/Al and Cu/Al for a given zeolite, has been identified as an important factor for achieving higher methanol yields (per mol Cu).[50,93] This proximity requirement is consistent with our finding that only 2Al configurations within Al−Al separations of <8.2 Å (CHA) and <9.4 Å (MOR) convert to dimers (Figure S5.1) at high temperatures. Therefore, our temperature-dependent MC simulations corroborate such monomer-to-dimer conversions and predict the majority of ZCuOH monomers will convert to dimers in the 600−900 K temperature range in both CHA and MOR. Kvande et al.[68] inferred (using in situ XAS during CO-TPR) that proximal ZCuOH may be depleted by ca. 673 K in MOR. Similarly, Pappas et al.[50] observed a gradual decrease in νCuOH from 523 to 673 K in CHA, and the ZCuOH population continued to slowly decrease when temperature was held at 673 K for 150 min. Although our MC simulations for both MOR and CHA predict a decrease in proximal ZCuOH pairs and $Z_2Cu_2(OH)_2$ populations in the same temperature range the above authors observe, our thermodynamic models suggest that conversion of these species to Z_2Cu_2O will continue past 673 K, and kinetic limitations for proximal ZCuOH to dimerize may play an important role.

Our simulation results at 10^{-6} kPa H_2O for CHA and MOR both predict $Z_2Cu_2(OH)_2$ persisting as the majority dimer species until ≈750 K, which is ≈100 K higher than conditions where Z_2Cu_2O has been reported the majority dimer species.[50,61,68,94] This discrepancy between the simulated and experimental temperatures for the transition between $Z_2Cu_2(OH)_2$ and Z_2Cu_2O likely reflects differences in the actual H_2O pressure for dry air treatments, which is challenging to quantify experimentally. Simulations spanning 10^{-4} to 10^{-10} kPa H_2O (Figure S6.6) show that Z_2Cu_2O becomes the majority species at 773 K when the H_2O pressure is $\lesssim 10^{-7}$ kPa and will require even lower temperatures to become the majority Cu species with a continued decrease in H_2O pressure. Thus, the trend of increasing Z_2Cu_2O populations with increasing temperature (and decreasing H_2O pressure) is consistent with many reports and may rationalize the need for high-temperature oxygen-activation treatments in PMO cycles.

Our MC model for Cu speciation makes two assumptions that may be violated due to kinetic factors or the presence of Cu^+. The population of peroxides ($Z_2Cu_2O_2$) is likely underestimated at lower temperatures because our model ignores kinetic limitations, so even if mechanistically peroxides form first and then convert to other species,[50,94,95] the peroxides could be trapped at lower temperatures before converting to more thermodynamically stable species at higher temperatures. At the highest temperatures, the population of peroxides increases due to the weak entropic driving force from the exchange reaction

$$Z_2H_2 + 2CuO(s) + \frac{1}{2}O_2 \xrightarrow{\Delta G_{Z_2Cu_2O_2}} Z_2Cu_2O_2 + H_2O \quad (8)$$

however, desorption of O_2 from Cu will also be entropically favored at high temperatures, potentially resulting in some amount of Cu^+

$$Z_2Cu_2O_2 \rightleftharpoons 2ZCu + O_2 \quad (9)$$

which is not captured in our model due to exclusion of Cu^+ species. Minority fractions of Cu^+ are commonly reported following high-temperature oxidative treatments. The mechanism and kinetics for this "autoreduction" phenomena are debated, but Cu speciation and proximity have been implicated as important factors.[8,96]

https://doi.org/10.1021/jacsau.3c00632
JACS Au 2024, 4, 197−215

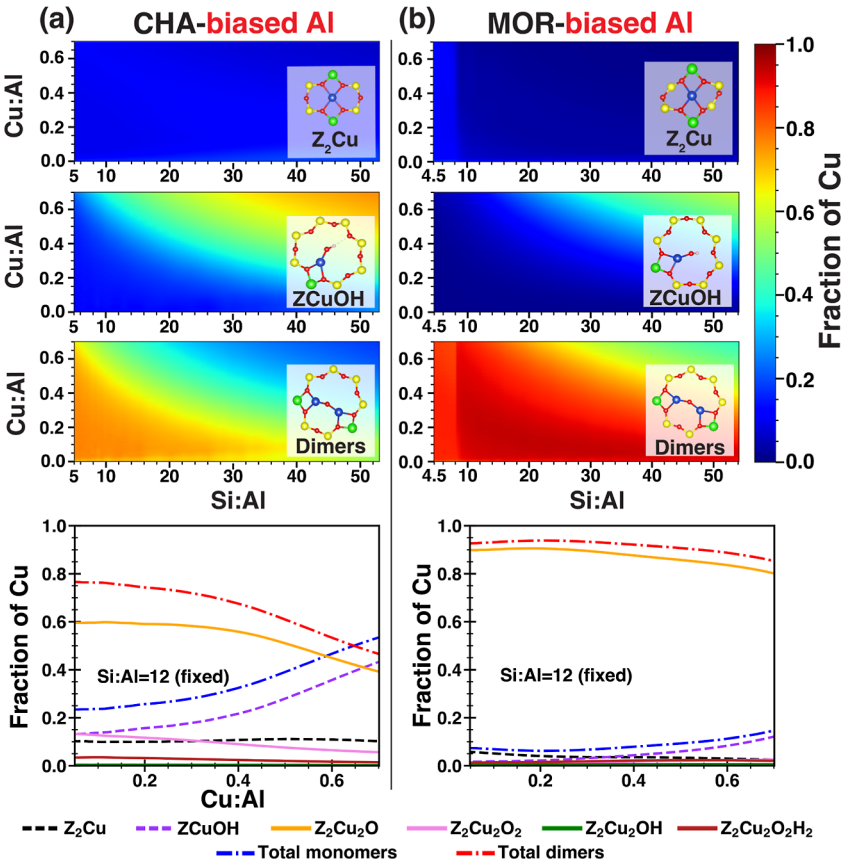

Figure 5. Predicted Cu speciation for biased Al distributions at conditions of 10^{-6} kPa H_2O, 20 kPa O_2 at 973 K for (a) CHA zeolite and (b) MOR zeolite as a function of material composition (Si/Al and Cu/Al). The Cu dimer heatmaps show the summation of all types of dimers, as shown in Figure 1c. Heatmaps in (b) show large gradients at Si/Al = 8 due to the different MOR Al biasing rules used for Si/Al < 8 and Si/Al > 8. Speciation of Cu-CHA and Cu-MOR with fixed Si/Al = 12 is shown in the bottom as a function of Cu/Al.

Cu Speciation for Nonrandom Al Distributions

Only certain zeolite types, such as CHA synthesized with specific protocols, evidence a pseudorandom aluminum distribution,[97,98] whereas zeolites such as commercial MOR commonly show nonrandom Al distributions.[99−102] The organic structure directing agents (SDAs), inorganic cations present in the synthesis media, and synthesis conditions (temperature and time) largely determine the Al distribution.[28,97,103,104] Although quantifying the populations of specific 2Al configurations remains a challenge, techniques such as Co^{2+} titration,[39,97] high-field ^{27}Al NMR,[80,105] and a combination of X-ray absorption and NMR[106] give information on macroscopic Al distributions. For nonrandom (biased) Al distributions, Cu speciation may change significantly due to changes in the populations of 2Al sites that have the most favorable exchange free energies. To test how biasing Al distributions affects Cu speciation, we chose several scenarios where experiments provide additional rules for Al-siting.

We ran MC simulations for CHA at 973 K (673 K simulations are in Section S6.1) that prohibit 2NN-6MR and 3NN-6MR 2Al configurations to populate (the lowest energy Cu exchange sites according to Figure 2a), still obey Löwenstein's rule, but otherwise populate Al randomly. The prohibition of these Al pairs has been observed following the synthesis of CHA with $TMAda^+$ in the absence of inorganic SDAs such as Na^+.[37,97] The probabilities used for MC simulations are the same as Figure 2a because the probability of dimer formation for a given 2Al configuration is independent of the macroscopic Al distribution and only depends on exchange conditions. However, Figure 5 shows that the absence of 2NN-6MR and 3NN-6MR configurations in the CHA lattice resulted in significantly higher total dimer fraction (60%−80% of total Cu) than in a random Al distributions (Figure 3) and a negligible amount of Z_2Cu (<10% of total Cu). The majority of (>95%) Z_2Cu that populate are in 2NN-8MR 2Al configurations (configuration 9 in Figure 2a) where dimer formation is only marginally exergonic (−4 kJ mol^{-1}) compared to monomer exchange, resulting in a nonzero Z_2Cu formation probability, and consequently a mixture of dimers and monomers exchange at this 2Al configuration. At Si/Al = 12 (Figure 3a-bottom), dimers populate in the CHA framework even at low Cu loadings (Cu/Al < 0.05), and as Cu loading increases, the total dimer fraction slowly declines at Cu/Al ≈ 0.35 due to the saturation of Al pairs that favor dimer formation and increasing population of ZCuOH. This Cu speciation pattern differs significantly from a random Al distribution CHA (Figure 3a) but is similar to that of a random Al distribution MOR (Figure 3b). Referring back to Figure 2a,b, once the first two 2Al configurations in CHA are eliminated, Cu is expected to occupy the next lowest energy 2Al configurations, which favor Cu dimers. This results in a macroscopic Cu speciation similar to MOR, but reaches a lower maximum dimer population.

In the second scenario, we ran MC simulations for MOR obeying Löwenstein's rule and prohibiting 2NN 2Al configurations, as observed for 5MR-containing zeolites with

https://doi.org/10.1021/jacsau.3c00632
JACS Au 2024, 4, 197−215

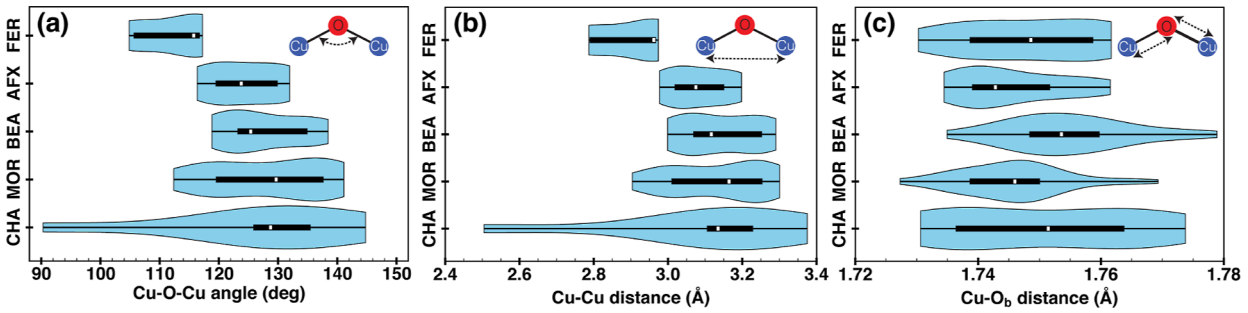

Figure 6. Geometric feature distributions for DFT-optimized Z_2Cu_2O (mono-μ-oxo) dimers in CHA, MOR, BEA, FER and AFX zeolites. (a) Cu−O−Cu angle, (b) Cu−Cu distance, and (c) Cu−O_b distance where O_b is the bridging oxygen between two Cu^{2+} ions. Above distributions only include Z_2Cu_2O dimers associated with 2Al configurations that preferentially exchange Cu as dimers, indicated by red squares in Figure 2a,b. Distributions including all dimers computed are shown in Section S10.1.

Si/Al > 8,[107−111] while constraining Al T-site occupancies to experimentally quantified populations for commercial MOR zeolites (Section S8.1).[99] Although different experimental methods[79,99,105] and calculations[101,112] show varying Al occupancy probabilities (5%−10% deviation), a similar trend in Al occupancy is reported: T3 (43%) > T4 (29%) > T1 (18%) > T2 (10%),[79,99,101,102,113] which are significantly different than the theoretical occupancies for a random Al distribution: T3 (16.7%) = T4 (16.7%) < T1 (33.3%) = T2 (33.3%). The abundance of Al in T3 and T4 sites and the absence of 2NN 2Al configurations (for Si/Al > 8) in the biased Al distribution gives a higher dimer population (Figure 5b) compared to a random Al distribution (Figure 3b). The most thermodynamically favored Cu exchange configuration in MOR is a 2Al T1-T2 pair that exchanges Z_2Cu, and the next most favorable exchange site is T4−T4, which exchanges Cu dimers. This preference is consistent with previous studies that show 2Al sites with T3−T3 and T4−T4 combinations form more stable Cu dimers than T1−T1 or T2−T2 combinations.[66,102,114] Therefore, increasing the %Al in T4 sites, and decreasing %Al in T1 and T2 sites, contribute to the observed increase of dimers. This effect is further enhanced by the increased multiplicity of other T3- and T4-containing 2Al configurations (Section S7) with slightly higher Cu dimer exchange energies (5−40 kJ mol^{-1}) than those discussed above because the abundance of such 2Al configurations makes those sites statistically favorable for Cu exchange. The biased Al distribution and higher multiplicity of dimer-preferred 2Al sites may enable MOR to reach close to the theoretical maximum methanol yield of 0.5 mol CH_3OH/mol Cu for Z_2Cu_2O sites, as observed by Pappas et al.[8] (0.47 mol CH_3OH/mol Cu). Biasing Al distributions could be a powerful synthetic strategy to increase the number of dimeric (or monomeric) Cu species in applications such as PMO, where binuclear sites are desirable. Both MOR and CHA Al biases considered above increase the dimer fraction, and notably, biasing the Al distribution causes CHA to behave similarly to MOR. Even within the same zeolite topology, Al distribution could alter the Cu speciation significantly such that zeolites with the same macroscopic Cu/Al and Si/Al may have dramatically different Cu nuclearities.

For BEA and FER MC simulations, we prohibited Al−O−Si−O−Al for Si/Al > 8, consistent with several studies,[107−109,115] while imposing Löwenstein's rule. However, for Si/Al < 8, we only applied Löwenstein's rule as those Si/Al ratios cannot mathematically be achieved without forming Al−O−Si−O−Al sequences. For BEA and FER, MC simulations for different experimentally observed Al biases are shown in Section S6.4. Al biases forcing 6MRs to contain a lower amount of Al than in a random Al distribution significantly increases the dimer population in BEA (Figure S6.4b,c) and FER (Figure S6.5a,b), similar to CHA. However, the elimination of Al from the T1 site in FER, consistent with the Al bias reported by Dědeček et al.[109] yields 100% monomers (Figure S6.5c). These results for BEA and FER reinforce that sample-specific Al distributions can strongly bias the Cu dimer population in a given zeolite.

Topology-Dependent Structural Features of Z_2Cu_2O

Geometric features of Cu dimers, such as Cu−O−Cu angle and Cu−Cu distance, are reported as important parameters for PMO activity[116−118] and potentially other reactions. Signatures of these geometric features are typically detected using resonance Raman (rR),[85,119] UV−vis,[68,102,117] and EXAFS.[68,91] To determine how zeolite topology influences geometric features of Z_2Cu_2O dimers, the most populous dimer species at high temperatures, we analyzed DFT-optimized Z_2Cu_2O structures in the five zeolite topologies: CHA, MOR, BEA, AFX, and FER. Experimentally detected distances (EXAFS) and angles are averaged over populated species, therefore, in our computational analysis (Figure 6), we exclude dimers that form at 2Al configurations that prefer monomer exchange. For completeness, we include geometric features of all DFT-computed Z_2Cu_2O structures in the Section S10.1.

The violin plots in Figure 6 report the distribution of Cu−O−Cu angles, and Cu−Cu/Cu−O_b distances (where O_b is the oxygen bridging two Cu) of Z_2Cu_2O structures. The Cu−O_b distances fall within a narrow range, and the Cu−Cu distances are strongly correlated with Cu−O−Cu angles. We observe a bimodal distribution of Cu−O−Cu angles centered at 120° and 140° for MOR, consistent with previous studies reporting a bimodal distribution for Cu−O−Cu species and angles[68,102,120] for MOR. These angles do not correlate with spin states, as both parts of the distribution have (Figure S10.2) a mix of singlet and triplet ground states. Vanelderen et al.[102] reported two distinct $[Cu−O−Cu]^{2+}$ sites in Cu-MOR by observing two absorption bands in their O_2-TPD experiments and rR spectra, and estimated Cu−O−Cu angles to be 137° ± 1° and 141° ± 1°, based on normal coordinate analysis of the rR vibrations. While we observe both of these Cu−O−Cu angles in our MOR distribution, the smaller Cu−O−Cu angles in our calculations are more skewed toward lower (≈120°) values, consistent with angles reported in their

https://doi.org/10.1021/jacsau.3c00632
JACS Au 2024, 4, 197−215

later study on MOR,[9] which could be a consequence of Al distribution. The Cu−O−Cu angles in CHA show a wider distribution, including 120° and 140° Z_2Cu_2O dimers[117] and one outlier at 90° at the 3NN-8MR 2Al configuration. The AFX, BEA, and FER zeolites show narrower Cu−O−Cu angle and Cu−Cu distance distributions compared to CHA and MOR, indicating that the populated dimer sites are more homogeneous in those zeolites.

Correlation between Cu Dimer Fractions and Methanol Yields

Although the methanol produced in cyclic PMO over different zeolites depends on the Al distribution, activation conditions,[19,55,88,121−125] and Cu-exchange protocol,[8,126−128] some zeolite topologies,[18,88,129] and specific compositions for a given topology, have generally been reported to have higher methanol per Cu yields. While we emphasize our goal here is not to determine specific active sites and activities for PMO, we next tested if observed trends in methanol yields correlate with our predicted total dimer populations. We used our MC predicted total Cu dimer fractions at 973 K, where dimer populations have largely saturated, as an upper bound for the total dimers in a zeolite sample with a specific Si/Al and Cu/Al. We used this number as a conservative upper-bound for the total dimer populations because the precise temperature for O_2 treatments varies, and as discussed above, analogous dimer populations are obtained at lower temperatures (673−973 K) with variation of H_2O pressures between 10^{-8} to 10^{-6} kPa. Further, higher CH_4 pressures are demonstrated[19,55,123] to increase the pool of active sites engaged, supporting the use of total dimer fractions as an upper bound.

Figure 7 shows the predicted equilibrium fraction of Cu dimers in CHA (random-Al distribution) and MOR (biased-Al

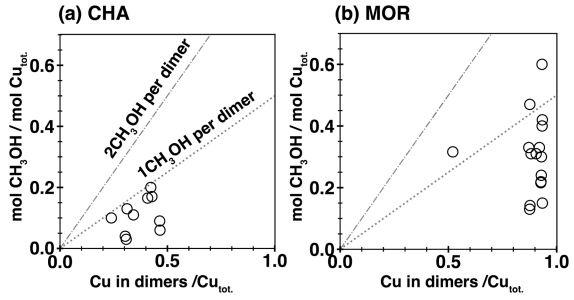

Figure 7. Experimentally reported mol CH_3OH/mol Cu versus the MC-predicted fraction of total Cu dimers at 10^{-6} kPa H_2O, 20 kPa O_2, 973 K for (a) CHA and (b) MOR. Details for the zeolite compositions and references corresponding to each data point are reported in Section S9.

distribution) versus experimentally reported mol CH_3OH/mol Cu in the literature (additional details in Section S9). We used a random Al distribution for CHA because the reported zeolites either used inorganic SDAs or were commercial samples. Similarly, the reported MOR samples are all commercial, so we used the biased Al distribution discussed above that is representative of many commercial MOR zeolites. For CHA, all reported mol CH_3OH/mol Cu fall near to or below the line demarcating 1 CH_3OH per predicted Cu dimer, showing a correlation between the maximum achievable mol CH_3OH/mol Cu as a function of composition (Si/Al and Cu/Al), and the predicted number of binuclear Cu sites at a given composition. With the exception of one data point with mol CH_3OH/mol Cu = 0.6, MOR data also fall near to or below the 1 CH_3OH per predicted Cu dimer threshold, but there is far less variation in the total dimer fraction at different Si/Al and Cu/Al ratios (Figure 5b). The majority of experimental data for both CHA and MOR fall well below the line demarcating one CH_3OH per predicted Cu dimer. This result suggests that in most samples only a fraction of the total binuclear Cu sites react with CH_4 to form CH_3OH at the reported O_2 and CH_4 activation conditions, consistent with the observations of many experimental reports.[8,57,61,68,130]

To compare across MOR, CHA, BEA, AFX, and FER, we used the most common Al distribution biases described in the literature for each zeolite along with Löwenstein's rule. Specifically, we prohibited Al−O−Si−O−Al configurations for MOR, BEA, and FER, used the Al T-siting bias described above for commercial MOR materials, and random Al distributions for CHA and AFX. Our simulations show that on the extreme ends, MOR has the highest fraction of Cu dimers at all compositions, and BEA has the lowest dimer population, which is consistent with the significantly lower PMO yields reported for BEA compared to CHA and MOR with similar compositions.[18,19,126,131] The mol CH_3OH/mol Cu values for AFX, FER, and BEA are again near to or below the line demarcating one CH_3OH per model-predicted binuclear Cu site (Figure S9.2). FER methanol yields[132] for a random Al distribution (Figure S9.3b) are far above this threshold, suggesting these FER materials do not contain Al−O−Si−O−Al configurations at Si/Al > 8, as reported by previous studies.[107,109] At a typical composition of Si/Al = 12, Cu/Al = 0.3, the ordering from most to least Cu dimers is MOR(0.92) ≫ CHA(0.45) > FER(0.34) > AFX(0.32) > BEA(0.28), consistent with the ordering of the maximum mol CH_3OH/mol Cu that is reported for these five zeolites at similar compositions[18,88,131] (Si/Al 8−15, Cu/Al 0.3−0.5) following cyclic PMO treatments. Caution is warranted for this comparison because of the uncertainty in Al distributions of these materials. Taken together, our results reinforce that the equilibrium population of higher nuclearity Cu species is a factor in determining the maximum achievable CH_3OH yields, however, under the vast majority of cyclic conditions and sample compositions not all of these higher nuclearity Cu sites may be kinetically accessible, reactive, or selective.

Classification of Zeolite Topologies

Differences in zeolite topologies create variations in Al−Al distances, ring sizes, T-site connectivities, and pore volumes, which may determine whether a specific 2Al exchange site populates with mononuclear or binuclear Cu sites. Our MC simulations show that zeolites with 8MRs have more 2Al pairs that exchange dimers (MOR, CHA, and AFX) compared to a zeolite with larger pores (BEA). We aimed to identify such patterns in Cu speciation in a high-throughput fashion using a machine learning model. Similar models have been reported for predictions of mechanical and chemical properties of zeolites and metal−organic frameworks,[133−135] 2D zeolite constructions,[136] zeolite-OSDA interactions governing synthesis,[104,137] and C−H activation barriers at $[Cu−O−Cu]^{2+}$ sites hosted in different zeolites.[118] The international zeolite database (IZDB) contains 254 zeolites[87] (composed of tetrahedral sites) that have been experimentally synthesized, and our goal is to screen these structures and identify zeolites with a strong preference for Cu monomers or dimers. To achieve this aim, we used our prior DFT results to build a

https://doi.org/10.1021/jacsau.3c00632
JACS Au 2024, 4, 197−215

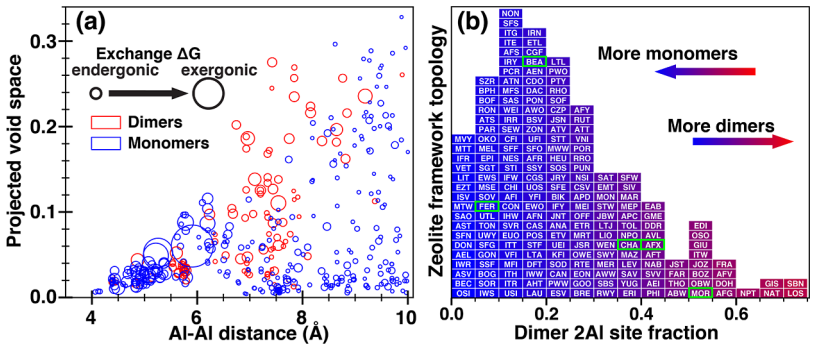

Figure 8. (a) Cu exchange free energy as a function of average projected void space and Al−Al distance for each 2Al configuration in the training and validation data set excluding Löwenstein's rule violations and Al−Al distances >10 Å. Larger circles represent more exergonic exchange free energies, and the colors show the identity of Cu species populated at the corresponding 2Al site. (b) Classification model-predicted number of symmetry distinct 2Al sites that preferentially exchange Cu as dimers divided by the total number of symmetry distinct 2Al sites, for 200 zeolites in the IZDB. The five zeolites used for model training and validation are highlighted with green boxes.

predictive model for dimer formation probabilities and applied it to zeolites in the IZDB.

To correlate structural features of a given 2Al site with the preference for that site to exchange Cu as a dimer or monomer, we trained an XGBoost decision tree binary classification model (detailed in Methods) using our DFT-computed dimer formation probabilities for five zeolites (CHA, MOR, AFX, BEA, and FER) as the targets of the classification model. Initially, as input descriptors, we used the Al−Al distance (Å) and the nearest neighbor connectivity (one plus the number of T atoms between Al−Al along the shortest path) corresponding to each 2Al configuration (within 10 Å) for all five zeolites, resulting in 318 total training data points (CHA-21 data points, MOR-100, BEA-154, AFX-43, and we held out FER-84 as a validation set). The DFT-computed dimer formation probabilities are rounded to 0 (monomer) or 1 (dimer) to generate the target for this binary model. With these simple descriptors, the model had 80% accuracy (10-fold cross-validation). We hypothesized that an important feature not captured by these descriptors is the volume of void space spanning 2Al. Corroborating our hypothesis, the accuracy of the model improved to 95% after adding void space descriptors, which we derived from random sphere packing in zeolite void space as described in the Methods section.

Feature importance scores (Figure S11.5) of the XGBoost model show the aggregate score (mean, min, max, and std. dev.) of the void space descriptors as the most discriminating feature of the model, followed by NN connectivity and Al−Al distances, which are similarly scored. Figure 8a reports the distance (Å) and void space (dimensionless) spanning each of the 318 2Al configurations used to train the model. Red and blue circles indicate preferential exchange of Cu dimers, or monomers, respectively, and the size of each circle reflects the exergonicity of the corresponding exchange reaction. The most stable Cu monomer exchange sites are clustered near Al−Al distances of 5−6 Å with low (0.05) void space, which correspond to exchange at the 6MRs present in all five zeolites, and monomer exchange at 4MRs and 5MRs is unfavorable. The most stable binuclear Cu sites generally fall into two clusters, 5−6 Å with low void space (analogous to monomers), and a broader cluster spanning ca. 7−8 Å and void space >0.1, roughly double the amount of void space needed for the most stable monomers. These two clusters are representative of the bimodal Cu−O−Cu angle distributions in MOR and BEA (Figure 6a), with the lower void space cluster accounting for the shorter Cu−O−Cu angle sites and the one 90° outlier structure in CHA.

Next, we made predictions using this binary classification model for 200 zeolites out of 254 zeolites in the IZDB, excluding 54 zeolites due to the high computational cost of generating graph-isomorphism-derived features for large supercells. For all unique 2Al configurations in each zeolite, the model predicts whether each 2Al configuration (within 10 Å) exchanges Cu as dimers or monomers. For example, there are 100 predictions for MOR (Figure 2b). Using these predictions, we defined a metric "Dimer 2Al Site Fraction (f)" that represents how many of those 2Al configurations favor Cu dimer formation

$$\text{dimer 2Al site fraction } (f) = \frac{\sum w_i\, p_{i,\text{dimer}}}{\sum w_i} \tag{10}$$

where w_i is the multiplicity of the ith 2Al configuration in the zeolite supercell based on the graph-isomorphism test (Methods and Section S1.1) and $p_{i,\text{dimer}}$ is the binary probability of dimer formation (0 for a monomer and 1 for a dimer) at 2Al configuration i, as predicted by the classification model.

Figure 8b shows the model predictions as a histogram, where zeolites have been sorted into $f = 0.05$ bins. The order of FER, BEA, CHA, AFX, and MOR is generally consistent with their MC simulation results, suggesting this is a reasonable approach for estimating nuclearity preferences for zeolite topologies. Zeolites sharing all SBUs generally appear together, for example, the CHA-AEI-AFT-AFX family of small pore zeolites all appear in the $f = 0.35-0.45$ regime. The majority of zeolites show $f \ll 0.5$, indicating that most known zeolites have higher populations of 2Al configurations that favor monomer exchange, likely a consequence of the commonality of 6MR SBUs across zeolites. At the extreme end, the zeolites OSI, BEC, ASV, and IWR have zero predicted 2Al configurations that favor dimer formation, indicating that they should only form mononuclear Cu sites, regardless of their Al distribution. These zeolites all have 6MRs and do not have 8MRs.

In contrast, zeolites favoring binuclear sites are rare, and none of the zeolites has $f = 1$, indicating that there will always be a possibility of Cu monomer formation. The model identified 2Al configurations in zeolite topologies with 8MRs and no 6MRs as the zeolites with the highest fraction of 2Al configurations that favor dimers, although we note that some

https://doi.org/10.1021/jacsau.3c00632
JACS Au 2024, 4, 197−215

of these topologies have not yet been synthesized as aluminosilicates, such as SBN. In zeolites that are not heavily biased toward monomers or dimers, the relative Cu exchange free energy rankings and Al distribution will play an important role in determining Cu speciation, and the descriptors used in this model are incapable of predicting accurate Cu exchange free energies. However, our results discern the important structural features of each zeolite's 2Al environments that lead to equilibrium Cu nuclearity biases and identify zeolite topologies on the extreme ends as candidates for further computational and experimental exploration.

CONCLUSIONS

MOR zeolites have been experimentally observed to have a high population of multinuclear Cu sites at a wide range of compositions (Si/Al and Cu/Al). Across all compositions, our Cu exchange free energies (computed using DFT energies) combined with MC simulations show that MOR has a higher equilibrium population of binuclear Cu sites than CHA, AFX, BEA, and FER due to two factors. First, MOR has a larger number of 2Al configurations than these other zeolites that preferentially exchange Cu dimers. Second, commercial MOR materials universally show Al-siting biases that reduce 2Al sites required for monomer exchange and increase the population of 2Al sites that are responsible for the lowest Cu dimer exchange free energies. The Al-siting bias for CHA to contain no 6MR 2Al configurations yields a higher fraction of Cu dimers than a random Al distribution and causes CHA to have Cu speciation that is more similar to MOR but with lower maximum dimer fractions. Such tunability of Cu speciation within the same zeolite topology via changing the Al distribution gives targets for rational design of SDAs that bias Al to specific T-sites.

Exposure conditions play an important role in Cu speciation. At ambient conditions, Cu will form H_2O-solvated $[Cu(H_2O)_4]^{2+}$ monomer complexes that are detached from the zeolite framework.[23] Increasing temperature and (or) decreasing H_2O pressure yields the heterogeneous distributions of Cu species explored here; however, even once Cu ions are bonded to the zeolite framework further condition-dependent speciation changes occur. Our MC simulations corroborated experimentally observed trends for proximal 2ZCuOH converting to Cu dimers at increasing temperatures (600−1000 K) through entropy-driven transformations of 2ZCuOH or $Z_2Cu_2(OH)_2$ to Z_2Cu_2O. The specific temperatures where these monomer−dimer or dimer−dimer conversions occur depend on the relative stability of each species at different 2Al configurations and subtle changes in H_2O pressure. Such conversions may rationalize the need for high-temperature oxygen-activation dry air treatments in PMO cycles. Further, comparisons with methanol yields (per Cu) in cyclic PMO, shows a general trend of increasing mol CH_3OH/mol Cu with increasing model-predicted total Cu dimer fractions for CHA at different compositions and in comparisons across different zeolite topologies. However, our results reinforce that the complexity of methane activation and methanol selectivity is unlikely to be explained by a single active site or set of conditions, and there are likely a distribution of active sites engaged, which depend on the Al distribution, reaction conditions, and Cu proximity and nuclearity.

Conversions between different Cu monomers, or monomers and dimers, may play an important role in the hydrothermal aging (HTA) of these materials at high temperatures and H_2O pressures, which is of critical importance for commercial SCR catalysts. Changes in Cu speciation have been observed following HTA treatments.[138−140] Our thermodynamic model-predicted depletion of ZCuOH sites at high temperatures is consistent with observations in these studies, however, capturing the microscopic details of speciation changes in HTA environments likely requires accounting for Al extraframework species and Al mobility.[140−143]

At equivalent exposure conditions, certain Al distributions and zeolite topologies show a preference for forming Cu monomers or dimers due to both structural features of the 2Al sites available, and the multiplicity of those 2Al sites. Dimer exchange probability calculations for all unique 2Al configurations in different zeolite topologies show that the majority of Cu dimers form at Al−Al distances ranging from 5 to 9 Å and require a higher void space between 2Al compared to monomers. These requisites lead to 8MRs and 10MRs promoting dimer formation across different zeolite topologies. Conversely, 6MRs promote monomer formation, and 4MRs and 5MRs are less favorable Cu exchange locations in general, because of steric repulsions. Due to the scope of the configurational space explored, our models do not address defect sites and higher nuclearity (>2 Cu) clusters;[144,145] however, similar structural requirements for local environments likely persist in these scenarios.

Our binary classification model showed that across 200 zeolites in the IZDB, most zeolites have more 2Al configurations that bias toward exchange of Cu monomers. This is because 6MRs, which are the ideal hosting environments for Z_2Cu monomers, are ubiquitous across the IZDB. Conversely, the minority populations of zeolites with 3MRs and 8MRs, or 8−10MRs and negligible 6MRs, have the highest population of 2Al configurations that thermodynamically prefer Cu dimers over monomers. Realization of aluminosilicate forms of some Cu dimer-biased zeolites with reasonable Si/Al ratios may be challenging, which presents an interesting conundrum. Zeolites with many 2Al configurations that exchange multinuclear Cu sites are rare, and similar geometric features to those used here may be useful for assessing the fidelity of hypothetical zeolites.[146] Further, the specific Al distribution of each zeolite and the relative exchange free energies for each 2Al site, which are not captured by this ML model, will be critical factors in determining Cu speciation. Although our analysis here specifically focused on Cu-zeolites, our methods are readily generalizable to other extraframework cations exchanged in zeolites that evince a distribution of nuclearities, such as Co, Pd, Ga, Mo, and Fe, to more broadly discern cation nuclearity preferences.

METHODS

Initial Structure Generation

To generate initial structures, we started by enumerating all symmetrically unique 2Al pairs for each selected zeolite topology. The zeolite unit cells, in their pure silica form, were obtained from the international zeolite association database (IZDB),[87] and we repeated the zeolite unit cell in each direction until all cell vectors were at least 10 Å. Next, for a given zeolite topology, we generated supercells containing each of the possible 2Al configurations (Z_2) with Al−Al distances within 10 Å. The choice of a 10 Å cutoff distance is justified because at longer distances, 2ZCuOH is more stable than Z_2Cu or Cu dimers (Section S5.3) for most 2Al configurations, and the % of 2Al sites populated by Z_2Cu and Cu dimers is negligible at longer (>9.4

https://doi.org/10.1021/jacsau.3c00632
JACS Au 2024, 4, 197−215

Å) Al−Al distances (Figure S5.1). Löwenstein's rule is the observation that Al−O−Al bond formation is unlikely to be observed in synthetic zeolites,[81] and therefore, Z_2 configurations with Al−O−Al were removed when enumerating 2Al configurations, except for CHA zeolite, which we kept Al−O−Al configurations for to benchmark relative Z_2Cu energies with previous work (these Al−O−Al structures are not used in the Results and Discussion sections).[27] To determine crystallographically unique 2Al configurations, we used a connectivity-based graph isomorphism test using the python NetworkX code.[147] This graph isomorphism test is a binary comparison,[148] where all 2Al substituted zeolite unit cells connectivity of Al and Si atoms were compared to each other. The graph isomorphism test significantly reduces the number of 2Al configurations; for example, for the 36 T site CHA cell, we initially generated 630 (36 choose 2) 2Al configurations and only 25 of those 630 2Al configurations are symmetrically distinct. We also retrieve the multiplicity of each unique 2Al configuration from the isomorphism test. For example, in the 36 T site CHA unit cell, the 6MR-2NN configuration statistically occurs 36 times, and 6MR-3NN configuration only occurs 18 times. From the isomorphism test, we record these multiplicities of each 2Al configuration and the indices of Al atoms that result in the same 2Al configuration.

To generate the initial structures for mononuclear Z_2Cu, ZCuOH, and binuclear ZCuOCuZ, $ZCuO_2CuZ$, ZCu(OH)CuZ, and $ZCu(OH)_2CuZ$, we first added the extraframework species to the symmetry unique 2Al configurations in zeolite unit cells. For Z_2Cu structures, the metal ion is placed inside a zeolite ring using the vector equation[27]

$$\mathbf{Al - Cu} = (\mathbf{Al - O_1}) + (\mathbf{Al - O_2}) \tag{11}$$

for each unique 2Al configuration. The bold letters indicate each atom's position vectors, and O_1 and O_2 are the oxygen atoms bonded to one of the Al under consideration. Figure 9a,b shows how this

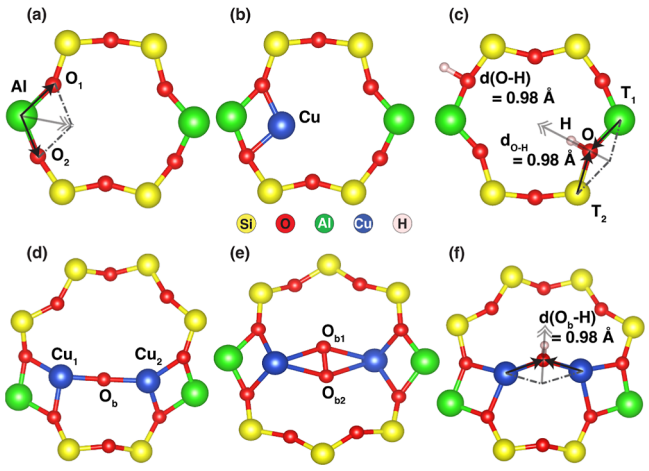

Figure 9. Initial geometry generation: (a) vector addition method and geometries generated for (b) Z_2Cu, (c) Z_2H_2, (d) Z_2Cu_2O, (e) $Z_2Cu_2O_2$, and (f) Z_2Cu_2OH using vector addition method. Atomic structures were visualized using the VESTA package.[149]

method places the Cu inside a zeolite ring on the same plane generated by $\mathbf{Al-O_1}$ and $\mathbf{Al-O_2}$. This method of generating initial guess Cu structures is repeated for every possible choice of bonded oxygen atoms, for example, the 2Al configuration in Figure 9a has four oxygen associated with each Al resulting in 12 initial Cu positions. We used another graph isomorphism test to remove similar Z_2Cu structures based on the connectivity of Cu, Al, and Si in the structure, for Figure 9a, this reduces the unique Cu locations to 6. We extended this vector addition method to generate initial structures for the species shown in Figure 9c−f and for ZCuOH, as discussed in Sections S1.2−S1.4, respectively.

High-Throughput Structure Screening

The above workflow results in numerous initial guess Cu structures for each 2Al configuration and each Cu motif. For the 2Al configuration in Figure 9a, before symmetry reduction 12 Z_2Cu, 36 ZCuOCuZ, 36 $ZCuO_2CuZ$, and 36 2ZCuOH structures are generated. For all 2Al configurations in CHA, 3000 total structures were generated, and 12,000 structures for MOR. After symmetry reduction, these numbers reduce to 2100 and 10,200 for CHA and MOR, respectively. To evaluate all of these structures with DFT would be computationally expensive and likely result in many unstable high-energy structures that may fail SCF-convergence. Thus, starting from the database of structures generated through vector addition, we optimized structures using two different force fields in series to downselect structures for spin-polarized DFT-optimizations (Scheme 1).

First, we performed global optimizations for all Z_2Cu, ZCuOCuZ, and $ZCuO_2CuZ$ structures using a physics-based interatomic potential that we developed (full details provided in Section S2) to determine energy and forces and basin hopping as the optimization algorithm[150,151] as implemented in the Python Scipy package.[152] Each structure from vector addition was input to basin hopping, and we obtained the global minima computed for each structure (still 2100 total structures for CHA). Subsequently, each of these structures, along with all of the vector addition-based structures for 2ZCuOH, was optimized to a local minimum using the FLARE[153] version 0.2.4 Gaussian process-based interatomic potentials that we trained individually for each Cu motif; full details of the method and training is in Section S3. Unlike the physics-based potential, the FLARE potential accurately predicts relative energy differences in Z_2Cu structures but is not effective for global optimization because it lacks training data representative of structures far from local minima. The lowest energy structures computed with FLARE for each Cu motif at a given 2Al configuration were then used as input structures for subsequent DFT calculations; additional structure selection details are reported in Section S3. For example, we optimized 6 symmetry distinct CHA-Z_2Cu structures using the physics-based potential followed by the FLARE potential and then picked the two lowest energy structures of the six for subsequent optimization with DFT. To downselect Cu dimer species, we checked the connectivity of each extraframework Cu motif and the zeolite framework. For example, in Z_2Cu_2O, we checked if Cu−O−Cu bonds were preserved, and no Si−O or Al−O bonds were broken in the zeolite framework. If either of these were violated, the structure was discarded. Altogether, filtering structures using this approach resulted in a significant reduction (3000 to 190 for CHA and 12,000 to 640 for MOR) in the number of initial guess structures for DFT calculations. We emphasize that all of the results reported in Results and Discussion use only DFT-computed energies.

We predicted the minimum energy Z_2H_2 structures for each 2Al configuration using the ZH energies computed for each symmetry unique T site and structural descriptors of vector addition-generated Z_2H_2 structures. Our model for predicting relative energies of Z_2H_2 structures (details in Section S4.3) is based on DFT calculations reported by Nystrom et al.,[154] where we use Al−Al and H−H distances evaluated before DFT-geometry optimization to estimate the relative energy of Z_2H_2. From this screening, we acquired the lowest energy Z_2H_2 structure for each unique 2Al site and then used DFT to optimize and obtain the energy of the selected Z_2H_2 structure. This method results in significant downsampling to approximately one structure input to DFT for every 16 Z_2H_2 structures generated.

We calculated the energies of all 2ZCuOH structures generated for CHA and MOR using DFT, and our results suggest that if Al−Al separation distances are >10 Å, the energy of exchanging Cu into two isolated ZH motifs to form 2ZCuOH is approximately equal to the energy of exchanging 2Cu at Z_2H_2 to form 2ZCuOH structures. Full details are reported in Section S4.4. Therefore, past 10 Å, we approximated 2ZCuOH exchange energies with 2× ZCuOH exchange free energies. For AFX, BEA, and FER, we used these mean-field

https://doi.org/10.1021/jacsau.3c00632
JACS Au 2024, 4, 197−215

Scheme 1. Workflow for Generating Structures for DFT Calculations; Initial Structure Generation, Sequentially Optimized Using the Physics-Based Force Field and Machine Learning Potential; Finally, DFT Calculations Are Used for Exchange Energy Evaluations

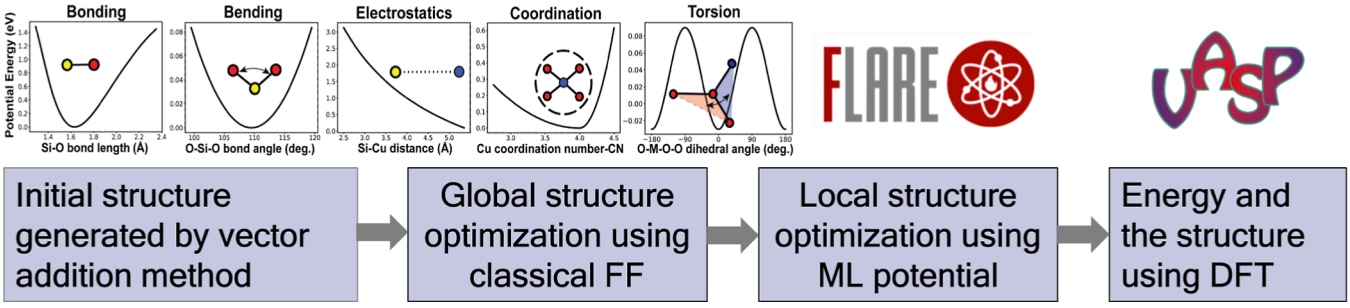

2ZCuOH energies computed for each T site pair instead of computing 2ZCuOH energies separately for each 2Al. The majority of ZCuOH structures optimize to 3-fold coordinated Cu centers, however, a minority of sites form 4-fold coordinated ZCuOH (with three bonds to extraframework oxygen), consistent with previously reported structures.[155]

DFT Calculations and Exchange Free Energies

To compute Cu exchange free energies ($\Delta G_{species}$) at each 2Al configuration, we optimized all the Z_2H_2, Cu monomer, and Cu dimer structures (selected from our structure screening described above) using the Vienna Ab Initio Simulation Package[156] (version 5.4.4). Structures files for optimized structures are provided as a Supporting Information attachment. Our spin-polarized DFT calculations used the projector-augmented wave[156,157] method of core valence interactions and a plane wave cutoff energy of 400 eV. The first Brillouin zone was sampled at the Γ point only, as appropriate for the large supercells (cell vectors for all zeolites multiplied until >10 Å) of these insulators. The generalized gradient approximation functional of Perdew–Burke–Ernzerhof (PBE)[158] was used to describe the exchange–correlation potential with the Becke–Johnson damping method [D3(BJ)vdw] included for dispersion corrections.[159,160] Motivated by recent literature reports,[161] and limitations in the accuracy of energies for some Cu-ion complexes computed using DFT,[62,161−163] we also tested the sensitivity of our predictions to PBE + U (Section S5.4) with a U parameter calibrated with crystalline Cu dimer compounds.[161] All electronic energies were converged to 10^{-6} eV and atomic forces to less than 0.03 eV/Å. Harmonic vibrational frequencies were computed with finite differences on atomic forces with displacements of 0.015 Å for all the atoms. Zero point vibrational energies (ZPE) were computed as

$$\mathrm{ZPE} = \sum_i \frac{1}{2} h\nu_i \tag{12}$$

To calculate the vibrational entropy of each dimeric and monomeric species ($Z_2Cu_xO_yH_z(s)$), we included frequencies >100 cm^{-1}, and frequencies <100 cm^{-1} were set to 100 cm^{-1}.[164]

$$S_{vib.} = -k_B \sum_i \ln(1 - e^{-h\nu_i/k_BT}) \tag{13}$$

To compute the exchange free energy of species ($\Delta G_{species}$), we used eq 1 and the DFT-computed (including ZPE's for all species) exchange reaction energy ($\Delta E_{x,y,z}$) computed as follows

$$\Delta E_{x,y,z} = E_{Z_2Cu_xO_yH_z(s)} - E_{Z_2H_2(s)} - xE_{CuO(s)} - \frac{(2y - 2x - z + 2)}{4} E_{O_2(g)} - \frac{(z-2)}{2} E_{H_2O(g)} \tag{14}$$

Treating the system as closed with respect to the Cu concentration gives the free energy as

$$\Delta G_{x,y,z} = \Delta E_{x,y,z} + \Delta \mathrm{ZPE}_{x,y,z} - T\Delta S_{vib.(x,y,z)} - x\Delta G_{CuO}(T) - \frac{(2y - 2x - z + 2)}{4} \Delta\mu_{O_2(g)}(T, P_{O_2}) - \frac{(z-2)}{2} \Delta\mu_{H_2O(g)}(T, P_{H_2O}) \tag{15}$$

where the chemical potentials $\Delta\mu_i$ of gas species and free energy of CuO ($\Delta G_{CuO}(T)$) are evaluated as follows

$$\Delta\mu_i = (G^\circ(T) - G^\circ(0\,\mathrm{K})) + k_BT \ln\left(\frac{P}{P^\circ}\right) \tag{16}$$

$$\Delta G_{CuO}(T) = G^\circ(T) - G^\circ(0\,\mathrm{K}) \tag{17}$$

using free energy values interpolated from the NIST JANAF thermochemical tables.[165]

To avoid many computationally expensive frequency calculations, we assumed $\Delta \mathrm{ZPE}_{x,y,z}$ and $S_{vib.(x,y,z)}$ are independent of 2Al configuration and zeolite topology and depend only on the specific Cu motif. To estimate the ZPE and $S_{vib.}$ corresponding to each Cu motif, a number of structures were sampled, these results show minimal variation for a given Cu motif and were averaged for use on other 2Al configurations (Section S5). Based on these calculations, we expect the errors introduced by assuming such 2Al configuration independence is negligible compared to the other terms such as $\Delta E_{x,y,z}$. The CuO(s) formation energy

$$\mathrm{Cu(s)} + \frac{1}{2}\mathrm{O_2(g)} \rightarrow \mathrm{CuO(s)} \tag{18}$$

is incorrectly predicted by the PBE (−131 kJ mol^{-1}) functional, and therefore, we corrected the energy of CuO such that it reproduces the experimentally reported formation enthalpy (−154 kJ mol^{-1}).[165] However, we did not apply this correction to our PBE + U calculations (Section S5.4), because the PBE + U functional more accurately predicted the CuO formation enthalpy (−152 kJ mol^{-1}). We compared exchange free energies obtained from PBE with PBE + U (with U = 6 eV[161] and all other parameters kept the same as PBE) and observed only minor changes in relative exchange free energies between the Cu motifs, as shown in Section S5.4.

Monte Carlo Simulations

To estimate the equilibrium fraction of different Cu species in a macroscopic zeolite system, we used Monte Carlo (MC) simulations based on the computed Cu exchange probabilities for each species at all 2Al sites in the corresponding zeolite supercell. The zeolite supercells used for our DFT calculations were repeated 3 × 3 × 3 times to improve the sampling of 2Al configurations.

For a given Si/Al ratio, we generated a 3 × 3 × 3 zeolite supercell and populated with Al up to the desired ratio, according to the rules described below. Subsequently, every possible 2Al configuration in the cell is enumerated, and relative probabilities for exchange of each of the six Cu motifs for each 2Al configuration are computed (eq 19).

https://doi.org/10.1021/jacsau.3c00632
JACS Au 2024, 4, 197−215

$$p_{i,s} = \frac{\exp\left(\frac{-\Delta G_{i,s}}{RT}\right)}{\sum_{i=1}^{N_{2Al\ config.}} \sum_{s}^{All\ Cu\ species} \exp\left(\frac{-\Delta G_{i,s}}{RT}\right)} \quad (19)$$

These probabilities are used to generate a weighted list of all possible Cu exchange events and a random number between 0 and 1 is chosen to select the exchange event, then the identity of Cu species and the 2Al configuration populated is recorded. Once a 2Al site is occupied by a dimer or monomer, we remove that Al pair from our 2Al list, generate a new probability list, and repeat the Cu exchange until all the 2Al sites in the zeolite are exhausted. For each Si/Al ratio, we averaged 20,000 independent MC simulations and created 1-D interpolations of the occupied Cu fraction as a function of Cu/Al for each species. Subsequently, all the 1-D interpolations for Si/Al = 3−55 were combined to generate the 2-D interpolations of species, as shown in Figure 3. We verified the convergence of our MC simulations by executing a separate MC simulation with 10,000 2Al configurations (Section S8).

When populating Al for our MC simulations, we excluded the 1NN 2Al configurations (Al−O−Al), obeying Löwenstein's rule.[81] Otherwise, each Al is populated randomly or follows a T site bias according to the required macroscopic T site occupancy by Al (Section S8.1). Sample code for the MC simulations has been provided as a Supporting Information attachment file.

Binary Classification Model for Predicting Dimer Formation

To identify the 2Al configurations for a given topology that favor Cu exchange as dimers, we trained an XGBoost[166] decision tree classification model. Based on the dimer formation probabilities ($p_{i,s}$) at Cu exchange conditions of 10^{-6} kPa H_2O, 20 kPa O_2 at 973 K, calculated using eq 5, we labeled all 2Al configurations in CHA, MOR, AFX, and BEA as 1 ($p_{i,s} \geq 0.5$) or 0 ($p_{i,s} < 0.5$). To generate the structural descriptors for the model, we used the Atomic Simulation Environment (ASE)[167] and NetworkX[147] python packages. For all unique 2Al configurations, Al−Al distances (in Å) in unoptimized zeolite cells and the nearest neighbor connectivity's (integer, refer to Section S11.1 for details) were generated as the first set of descriptors for the classification model.

We generated the second set of descriptors using random sphere packing to improve the classification accuracy. We sample the zeolite void space by randomly placing points in the zeolite unit cell with an average density of 1 point $Å^{-3}$. Then, we removed all points within 2.0 Å of framework atoms, thereby only retaining points that fill the zeolite void space (Figure S11.1). This 2.0 Å cutoff was chosen to capture Cu-framework oxygen interactions where Cu−O bonds are ≈1.95 Å.[27,60] We derived a custom descriptor, "projected void space" defined as

$$\text{Projected void space} = \sum_{\text{mid (Al−Al) to sphere distance } (d)}^{\text{All random spheres retained}} e^{(-\alpha d)} \quad (20)$$

to capture the nature of the random packing, where d is the distance measured from the bisection point of Al−Al to all the random spheres retained, and α is a hyperparameter for the projection. Additional details and figures for this approach are located in Section S11.1. Statistics (minimum, maximum, average, and standard deviation) of the projected void space were generated from 2000 independent random sphere packing simulations for each 2Al configuration. Al−Al distance, nearest neighbor connectivity, and statistics of random sphere packing were used as features in our classification model. Therefore, our training data set consists of six descriptors and 318 data points (CHA-21, MOR-100, BEA-154, AFX-43), and FER data was held out as a validation set.

We used the XGBoost classifier as implemented in the open source Python code from Chen et al.[168] because boosting tree algorithms have proven robust for small data sets.[169,170] The hyperparameters of the XGBoost model and α in void space projection were optimized using grid searches (Section S11). The 10-fold cross-validation accuracy of the model was used as the metric for comparing different models. More details on hyperparameter optimization and model accuracy can be found in Section S11. The training data set has more 2Al sites that favor monomer formation (69.5% of 2Al) than dimers (30.5% of 2Al), indicating a mild class imbalance. Therefore, we tested ML models with and without adjusting for class imbalance (Section S11.3) and found similar performance for both models.

To identify the features that are the most important when deciding a 2Al configuration's dimer (or monomer) preference, we used the "feature importance score", defined as how many times a feature is selected for splitting (making a decision), weighted by the squared improvement of the model gained by each split, and averaged over all trees.[171,172] The final XGBoost model is provided as a Supporting Information attachment file.

■ ASSOCIATED CONTENT

Supporting Information

The Supporting Information is available free of charge at https://pubs.acs.org/doi/10.1021/jacsau.3c00632.

ZIP file containing DFT-optimized structure files, sample Python codes for MLP training and optimized parameters for physics-based force field, sample code for MC simulations, and optimized XGBoost model (ZIP)

Initial structure generation, physics-based forcefield training and optimization, MLP, structure selection and optimization, MC simulation, convergence, functional comparison, geometric structure and electron spin analysis, and classification model details (PDF)

■ AUTHOR INFORMATION

Corresponding Author

Christopher Paolucci − *Department of Chemical Engineering, University of Virginia, Charlottesville, Virginia 22903, United States;* orcid.org/0000-0002-4506-9306; Email: cp9wx@virginia.edu

Authors

Asanka Wijerathne − *Department of Chemical Engineering, University of Virginia, Charlottesville, Virginia 22903, United States;* orcid.org/0000-0003-1339-7812

Allison Sawyer − *Department of Chemical Engineering, University of Virginia, Charlottesville, Virginia 22903, United States*

Rohil Daya − *Cummins Inc, Columbus, Indiana 47201, United States;* orcid.org/0000-0002-9916-1052

Complete contact information is available at: https://pubs.acs.org/10.1021/jacsau.3c00632

Notes

The authors declare no competing financial interest.

■ ACKNOWLEDGMENTS

The authors acknowledge Cummins Inc. for financial support. The authors are grateful to Ms. Anna Sviripa (UVA) for her guidance in setting up the Machine Learning Potential used in high-throughput screening. The authors thank the University of Virginia's Research Computing for computational resources, Prof. William S. Epling (UVA), Prof. Robert J. Davis (UVA), Prof. William F. Schneider (Notre Dame), and Prof. Rajamani Gounder (Purdue) for helpful technical discussions.

REFERENCES

(1) Kosinov, N.; Liu, C.; Hensen, E. J. M.; Pidko, E. A. Engineering of Transition Metal Catalysts Confined in Zeolites. *Chem. Mater.* **2018**, *30*, 3177−3198.

(2) Back, S.; Yeom, M. S.; Jung, Y. Active Sites of Au and Ag Nanoparticle Catalysts for CO2 Electroreduction to CO. *ACS Catal.* **2015**, *5*, 5089−5096.

(3) Li, G.; Pidko, E. A. The Nature and Catalytic Function of Cation Sites in Zeolites: a Computational Perspective. *ChemCatChem* **2019**, *11*, 134−156.

(4) Lamberti, C.; Beato, P.; Svelle, S.; Olsbye, U.; Borfecchia, E.; Bordiga, S.; Lamberti, C. Cu-CHA-a model system for applied selective redox catalysis. *Chem. Soc. Rev.* **2018**, *47*, 8097−8133.

(5) Li, H.; Yu, B.; Zhuang, Z.; Sun, W.; Jia, B.; Ma, T. A small change in the local atomic environment for a big improvement in single-atom catalysis. *J. Mater. Chem. A* **2021**, *9*, 4184−4192.

(6) Zambelli, T.; Wintterlin, J.; Trost, J.; Ertl, G. Identification of the 'active sites' of a surface-catalyzed reaction. *Science* **1996**, *273*, 1688−1690.

(7) Lei, Y.; Wang, Y.; Liu, Y.; Song, C.; Li, Q.; Wang, D.; Li, Y. Designing Atomic Active Centers for Hydrogen Evolution Electrocatalysts. *Angew. Chem., Int. Ed.* **2020**, *59*, 20794−20812.

(8) Pappas, D. K.; Martini, A.; Dyballa, M.; Kvande, K.; Teketel, S.; Lomachenko, K. A.; Baran, R.; Glatzel, P.; Arstad, B.; Berlier, G.; et al. The Nuclearity of the Active Site for Methane to Methanol Conversion in Cu-Mordenite: A Quantitative Assessment. *J. Am. Chem. Soc.* **2018**, *140*, 15270−15278.

(9) Snyder, B. E. R.; Vanelderen, P.; Schoonheydt, R. A.; Sels, B. F.; Solomon, E. I. Second-Sphere Effects on Methane Hydroxylation in Cu-Zeolites. *J. Am. Chem. Soc.* **2018**, *140*, 9236−9243.

(10) Nunthakitgoson, W.; Thivasasith, A.; Maihom, T.; Wattanakit, C. Effects of single and double active sites of Cu oxide clusters over the MFI zeolite for direct conversion of methane to methanol: DFT calculations. *Phys. Chem. Chem. Phys.* **2021**, *23*, 2500−2510.

(11) Khurana, I.; Albarracin-Caballero, J. D.; Shih, A. J. Identification and quantification of multinuclear Cu active sites derived from monomeric Cu moieties for dry NO oxidation over Cu-SSZ-13. **2022**, *413*, 1111−1122, .

(12) Rong, H.; Ji, S.; Zhang, J.; Wang, D.; Li, Y. Synthetic strategies of supported atomic clusters for heterogeneous catalysis. *Nat. Commun.* **2020**, *11*, 5884.

(13) Lu, J.; Serna, P.; Aydin, C.; Browning, N. D.; Gates, B. C. Supported Molecular Iridium Catalysts: Resolving Effects of Metal Nuclearity and Supports as Ligands. *J. Am. Chem. Soc.* **2011**, *133*, 16186−16195.

(14) Wang, Q.; Pengmei, Z.; Pandharkar, R.; Gagliardi, L.; Hupp, J. T.; Notestein, J. M. Investigating the effect of metal nuclearity on activity for ethylene hydrogenation by metal-organic-framework-supported oxy-Ni(II) catalysts. *J. Catal.* **2022**, *407*, 162−173.

(15) Martin, G. A. Variation of the number of metal atoms involved in active sites and of the true activation energy of hydrocarbon conversion and co hydrogenation over metals. *Bull. Soc. Chim. Belg.* **1996**, *105*, 131−137.

(16) Snyder, B. E.; Bols, M. L.; Schoonheydt, R. A.; Sels, B. F.; Solomon, E. I. Iron and Copper Active Sites in Zeolites and Their Correlation to Metalloenzymes. *Chem. Rev.* **2018**, *118*, 2718−2768.

(17) Newton, M. A.; Knorpp, A. J.; Pinar, A. B.; Sushkevich, V. L.; Palagin, D.; van Bokhoven, J. A. On the Mechanism Underlying the Direct Conversion of Methane to Methanol by Copper Hosted in Zeolites; Braiding Cu K-Edge XANES and Reactivity Studies. *J. Am. Chem. Soc.* **2018**, *140*, 10090−10093.

(18) Newton, M. A.; Knorpp, A. J.; Sushkevich, V. L.; Palagin, D.; van Bokhoven, J. A. Active sites and mechanisms in the direct conversion of methane to methanol using Cu in zeolitic hosts: a critical examination. *Chem. Soc. Rev.* **2020**, *49*, 1449−1486.

(19) Knorpp, A. J.; Pinar, A. B.; Newton, M. A.; Sushkevich, V. L.; van Bokhoven, J. A. Copper-Exchanged Omega (MAZ) Zeolite: Copper-concentration Dependent Active Sites and its Unprecedented Methane to Methanol Conversion. *ChemCatChem* **2018**, *10*, 5593−5596.

(20) Tomkins, P.; Ranocchiari, M.; van Bokhoven, J. A. Direct Conversion of Methane to Methanol under Mild Conditions over Cu-Zeolites and beyond. *Acc. Chem. Res.* **2017**, *50*, 418−425.

(21) Li, S.; Wang, Y.; Wu, T.; Schneider, W. F. First-Principles Analysis of Site- and Condition-Dependent Fe Speciation in SSZ-13 and Implications for Catalyst Optimization. *ACS Catal.* **2018**, *8*, 10119−10130.

(22) Snyder, B. E. R.; Vanelderen, P.; Bols, M. L.; Hallaert, S. D.; Bottger, L. H.; Ungur, L.; Pierloot, K.; Schoonheydt, R. A.; Sels, B. F.; Solomon, E. I. The active site of low-temperature methane hydroxylation in iron-containing zeolites. *Nature* **2016**, *536*, 317−321.

(23) Paolucci, C.; Di Iorio, J. R.; Schneider, W. F.; Gounder, R. Solvation and mobilization of copper active sites in zeolites by ammonia: Consequences for the catalytic reduction of nitrogen oxides. *Acc. Chem. Res.* **2020**, *53*, 1881−1892.

(24) Gao, F.; Kwak, J. H.; Szanyi, J.; Peden, C. H. F.; Peden, H. F. Current Understanding of Cu-Exchanged Chabazite Molecular Sieves for Use as Commercial Diesel Engine DeNO x Catalysts. *Top. Catal.* **2013**, *56*, 1441−1459.

(25) Verma, A. A.; Bates, S. A.; Anggara, T.; Paolucci, C.; Parekh, A. A.; Kamasamudram, K.; Yezerets, A.; Miller, J. T.; Delgass, W. N.; Schneider, W. F.; Ribeiro, F. H. NO oxidation: A probe reaction on Cu-SSZ-13. *J. Catal.* **2014**, *312*, 179−190.

(26) Sazama, P.; Tabor, E.; Klein, P.; Wichterlova, B.; Sklenak, S.; Mokrzycki, L.; Pashkkova, V.; Ogura, M.; Dedecek, J. Al-rich beta zeolites. Distribution of Al atoms in the framework and related protonic and metal-ion species. *J. Catal.* **2016**, *333*, 102−114.

(27) Li, S.; Li, H.; Gounder, R.; Debellis, A.; Müller, I. B.; Prasad, S.; Moini, A.; Schneider, W. F. First-Principles Comparison of Proton and Divalent Copper Cation Exchange Energy Landscapes in SSZ-13 Zeolite. *J. Phys. Chem. C* **2018**, *122*, 23564−23573.

(28) Nimlos, C. T.; Hoffman, A. J.; Hur, Y. G.; Lee, B. J.; Di Iorio, J. R.; Hibbitts, D. D.; Gounder, R. Experimental and Theoretical Assessments of Aluminum Proximity in MFI Zeolites and Its Alteration by Organic and Inorganic Structure-Directing Agents. *Chem. Mater.* **2020**, *32*, 9277−9298.

(29) Mandal, K.; Gu, Y.; Westendorff, K. S.; Li, S.; Pihl, J. A.; Grabow, L. C.; Epling, W. S.; Paolucci, C. Condition-Dependent Pd Speciation and NO adsorption in Pd/Zeolites. *ACS Catal.* **2020**, *10*, 12801−12818.

(30) Mortier, W. J. A Statistical Thermodynamical Approach to the Distribution of Cations in Silicate Minerals. *J. Phys. Chem.* **1975**, *79*, 1447−1449.

(31) Paolucci, C.; Parekh, A. A.; Khurana, I.; Di Iorio, J. R.; Li, H.; Albarracin Caballero, J. D.; Shih, A. J.; Anggara, T.; Delgass, W. N.; Miller, J. T.; Ribeiro, F. H.; Gounder, R.; Schneider, W. F. Catalysis in a cage: Condition-dependent speciation and dynamics of exchanged Cu cations in SSZ-13 zeolites. *J. Am. Chem. Soc.* **2016**, *138*, 6028−6048.

(32) Göltl, F.; Bhandari, S.; Mavrikakis, M. Thermodynamics Perspective on the Stepwise Conversion of Methane to Methanol over Cu-Exchanged SSZ-13. *ACS Catal.* **2021**, *11*, 7719−7734.

(33) Dinh, K. T.; Sullivan, M. M.; Narsimhan, K.; Serna, P.; Meyer, R. J.; Dincă, M.; Román-Leshkov, Y. Continuous Partial Oxidation of Methane to Methanol Catalyzed by Diffusion-Paired Copper Dimers in Copper-Exchanged Zeolites. *J. Am. Chem. Soc.* **2019**, *141*, 11641−11650.

(34) Hu, W.; Iacobone, U.; Gramigni, F.; Zhang, Y.; Wang, X.; Liu, S.; Zheng, C.; Nova, I.; Gao, X.; Tronconi, E. Unraveling the Hydrolysis of Z2Cu2+to ZCu2+(OH)-and Its Consequences for the Low-Temperature Selective Catalytic Reduction of NO on Cu-CHA Catalysts. *ACS Catal.* **2021**, *11*, 11616−11625.

(35) Engedahl, U.; Grönbeck, H.; Hellman, A. First-Principles Study of Oxidation State and Coordination of Cu-Dimers in Cu-SSZ-13 during Methane-to-Methanol Reaction Conditions. *J. Phys. Chem. C* **2019**, *123*, 26145−26150.

https://doi.org/10.1021/jacsau.3c00632
JACS Au 2024, 4, 197−215

(36) Dědeček, J.; Tabor, E.; Sklenak, S. Tuning the Aluminum Distribution in Zeolites to Increase their Performance in Acid-Catalyzed Reactions. *ChemSusChem* **2019**, *12*, 556−576.
(37) Di Iorio, J. R.; Li, S.; Jones, C. B.; Nimlos, C. T.; Wang, Y.; Kunkes, E.; Vattipalli, V.; Prasad, S.; Moini, A.; Schneider, W. F.; Gounder, R. Cooperative and Competitive Occlusion of Organic and Inorganic Structure-Directing Agents within Chabazite Zeolites Influences Their Aluminum Arrangement. *J. Am. Chem. Soc.* **2020**, *142*, 4807−4819.
(38) Barthomeuf, D. Zeolite acidity dependence on structure and chemical environment. Correlations with catalysis. *Mater. Chem. Phys.* **1987**, *17*, 49−71.
(39) Dêdeček, J.; Gábová, V.; Wichterlová, B. The effect of dealumination on the Al distribution in pentasil ring zeolites. *Stud. Surf. Sci. Catal.* **2002**, *142*, 1817−1824.
(40) del Campo, P.; Beato, P.; Rey, F.; Navarro, M. T.; Olsbye, U.; Lillerud, K. P.; Svelle, S. Influence of post-synthetic modifications on the composition, acidity and textural properties of ZSM-22 zeolite. *Catal. Today* **2018**, *299*, 120−134.
(41) Kwak, S. J.; Kim, H. S.; Park, N.; Park, M. J.; Lee, W. B. Recent progress on Al distribution over zeolite frameworks: Linking theories and experiments. *Korean J. Chem. Eng.* **2021**, *38*, 1117−1128.
(42) Weitkamp, J. Zeolites and catalysis. *Solid State Ionics* **2000**, *131*, 175−188.
(43) Brus, J.; Kobera, L.; Schoefberger, W.; Urbanová, M.; Klein, P.; Sazama, P.; Tabor, E.; Sklenak, S.; Fishchuk, A. V.; Dědeček, J. Structure of framework aluminum lewis sites and perturbed aluminum atoms in zeolites as determined by $^{27}Al\{^{1}H\}$ REDOR (3Q) MAS NMR spectroscopy and DFT/molecular mechanics. *Angew. Chem., Int. Ed.* **2015**, *54*, 541−545.
(44) Borfecchia, E.; Lomachenko, K. A.; Giordanino, F.; Falsig, H.; Beato, P.; Soldatov, A. V.; Bordiga, S.; Lamberti, C. Revisiting the nature of Cu sites in the activated Cu-SSZ-13 catalyst for SCR reaction. *Chem. Sci.* **2015**, *6*, 548−563.
(45) Beale, A. M.; Gao, F.; Lezcano-Gonzalez, I.; Peden, C. H. F.; Szanyi, J. Recent advances in automotive catalysis for NOx emission control by small-pore microporous materials. *Chem. Soc. Rev.* **2015**, *44*, 7371−7405.
(46) Liu, L. C.; Corma, A. Confining isolated atoms and clusters in crystalline porous materials for catalysis. *Nat. Rev. Mater.* **2020**, *6*, 244−263.
(47) Godiksen, A.; Stappen, F. N.; Vennestrøm, P. N. R.; Giordanino, F.; Rasmussen, S. B.; Lundegaard, L. F.; Mossin, S. Coordination environment of copper sites in Cu-CHA zeolite investigated by electron paramagnetic resonance. *J. Phys. Chem. C* **2014**, *118*, 23126−23138.
(48) Martini, A.; Borfecchia, E.; Lomachenko, K. A.; Pankin, I. A.; Negri, C.; Berlier, G.; Beato, P.; Falsig, H.; Bordiga, S.; Lamberti, C. Composition-driven Cu-speciation and reducibility in Cu-CHA zeolite catalysts: a multivariate XAS/FTIR approach to complexity. *Chem. Sci.* **2017**, *8*, 6836−6851.
(49) Vanelderen, P.; Vancauwenbergh, J.; Sels, B. F.; Schoonheydt, R. A. Coordination chemistry and reactivity of copper in zeolites. *Coord. Chem. Rev.* **2013**, *257*, 483−494.
(50) Pappas, D. K.; Borfecchia, E.; Dyballa, M.; Pankin, I. A.; Lomachenko, K. A.; Martini, A.; Signorile, M.; Teketel, S.; Arstad, B.; Berlier, G.; et al. Methane to Methanol: Structure-Activity Relationships for Cu-CHA. *J. Am. Chem. Soc.* **2017**, *139*, 14961−14975.
(51) Wulfers, M. J.; Teketel, S.; Ipek, B.; Lobo, R. F. Conversion of methane to methanol on copper-containing small-pore zeolites and zeotypes. *Chem. Commun.* **2015**, *51*, 4447−4450.
(52) Park, M. B.; Ahn, S. H.; Mansouri, A.; Ranocchiari, M.; van Bokhoven, J. A. Comparative Study of Diverse Copper Zeolites for the Conversion of Methane into Methanol. *ChemCatChem* **2017**, *9*, 3705−3713.
(53) Sushkevich, V. L.; Artsiusheuski, M.; Klose, D.; Jeschke, G.; van Bokhoven, J. A. Identification of Kinetic and Spectroscopic Signatures of Copper Sites for Direct Oxidation of Methane to Methanol. *Angew. Chem., Int. Ed.* **2021**, *60*, 15944−15953.
(54) Grundner, S.; Markovits, M. A. C.; Li, G.; Tromp, M.; Pidko, E. A.; Hensen, E. J. M.; Jentys, A.; Sanchez-Sanchez, M.; Lercher, J. A. Single-site trinuclear copper oxygen clusters in mordenite for selective conversion of methane to methanol. *Nat. Commun.* **2015**, *6*, 7546.
(55) Brezicki, G.; Kammert, J. D.; Gunnoe, T. B.; Paolucci, C.; Davis, R. J. Insights into the Speciation of Cu in the Cu-H-Mordenite Catalyst for the Oxidation of Methane to Methanol. *ACS Catal.* **2019**, *9*, 5308−5319.
(56) Fischer, J. W. A.; Brenig, A.; Klose, D.; van Bokhoven, J. A.; Sushkevich, V. L.; Jeschke, G. Methane Oxidation over Cu^{2+}/$[CuOH]^{+}$ Pairs and Site-Specific Kinetics in Copper Mordenite Revealed by Operando Electron Paramagnetic Resonance and UV/Visible Spectroscopy. *Angew. Chem., Int. Ed.* **2023**, *135*, No. e202303574.
(57) Oord, R.; Schmidt, J. E.; Weckhuysen, B. M. Methane-to-methanol conversion over zeolite Cu-SSZ-13, and its comparison with the selective catalytic reduction of NOx with NH3. *Catal. Sci. Technol.* **2018**, *8*, 1028−1038.
(58) Daya, R.; Deka, D. J.; Goswami, A.; Menon, U.; Trandal, D.; Partridge, W. P.; Joshi, S. Y. A redox model for NO oxidation, NH_3 oxidation and high temperature standard SCR over Cu-SSZ-13. *Appl. Catal., B* **2023**, *328*, 122524.
(59) Paolucci, C.; Di Iorio, J.; Ribeiro, F.; Gounder, R.; Schneider, W. *In Chapter One - Catalysis Science of NOx Selective Catalytic Reduction With Ammonia Over Cu-SSZ-13 and Cu-SAPO-34*; Song, C., Ed.; *Advances in Catalysis*; Academic Press, 2016; Vol. *59*, pp 1−107.
(60) Göltl, F.; Hafner, J. Structure and properties of metal-exchanged zeolites studied using gradient-corrected and hybrid functionals. I. Structure and energetics. *J. Chem. Phys.* **2012**, *136*, 064501.
(61) Alayon, E. M. C.; Nachtegaal, M.; Bodi, A.; Ranocchiari, M.; van Bokhoven, J. A. Bis(μ-oxo) versus mono(μ-oxo)dicopper cores in a zeolite for converting methane to methanol: an in situ XAS and DFT investigation. *Phys. Chem. Chem. Phys.* **2015**, *17*, 7681−7693.
(62) Kulkarni, A. R.; Zhao, Z.-J.; Siahrostami, S.; Nørskov, J. K.; Studt, F. Monocopper Active Site for Partial Methane Oxidation in Cu-Exchanged 8MR Zeolites. *ACS Catal.* **2016**, *6*, 6531−6536.
(63) Turnes Palomino, G.; Fisicaro, P.; Bordiga, S.; Zecchina, A.; Giamello, E.; Lamberti, C. Oxidation States of Copper Ions in ZSM-5 Zeolites. A Multitechnique Investigation. *J. Phys. Chem. B* **2000**, *104*, 4064−4073.
(64) Ipek, B.; Wulfers, M. J.; Kim, H.; Göltl, F.; Hermans, I.; Smith, J. P.; Booksh, K. S.; Brown, C. M.; Lobo, R. F. Formation of $[Cu_2O_2]^{2+}$and $[Cu_2O]^{2+}$toward C−H Bond Activation in Cu-SSZ-13 and Cu-SSZ-39. *ACS Catal.* **2017**, *7*, 4291−4303.
(65) Göltl, F.; Bhandari, S.; Lebrón-Rodríguez, E. A.; Gold, J. I.; Zones, S. I.; Hermans, I.; Dumesic, J. A.; Mavrikakis, M. Identifying hydroxylated copper dimers in SSZ-13 via UV-vis-NIR spectroscopy. *Catal. Sci. Technol.* **2022**, *12*, 2744−2748.
(66) Brezicki, G.; Zheng, J.; Paolucci, C.; Schlögl, R.; Davis, R. J. Effect of the Co-cation on Cu Speciation in Cu-exchanged mordenite and ZSM-5 catalysts for the oxidation of methane to methanol. *ACS Catal.* **2021**, *11*, 4973−4987.
(67) Guan, X.; Xu, Z.; Du, H.; Liu, X.; Yan, P.; Guo, X.; Zhang, Z. C. Increase the number of active sites in Cu-MOR through NO/NH_3 pretreatment for catalytic oxidation of methane to methanol. *Catal. Commun.* **2022**, *163*, 106411.
(68) Kvande, K.; Garetto, B.; Deplano, G.; Signorile, M.; Solemsli, B. G.; Prodinger, S.; Olsbye, U.; Beato, P.; Bordiga, S.; Svelle, S.; Borfecchia, E. Understanding C−H activation in light alkanes over Cu-MOR zeolites by coupling advanced spectroscopy and temperature-programmed reduction experiments. *Chem. Sci.* **2023**, *14*, 9704−9723.
(69) Fickel, D. W.; Lobo, R. F. Copper Coordination in Cu-SSZ-13 and Cu-SSZ-16 Investigated by Variable-Temperature XRD. *J. Phys. Chem. C* **2010**, *114*, 1633−1640.
(70) Göltl, F.; Bulo, R. E.; Hafner, J. R.; Sautet, P. What Makes Copper-Exchanged SSZ-13 Zeolite Efficient at Cleaning Car Exhaust Gases? *J. Phys. Chem. Lett.* **2013**, *4*, 2244−2249.

https://doi.org/10.1021/jacsau.3c00632
JACS Au 2024, 4, 197−215

(71) Li, H.; Paolucci, C.; Khurana, I.; Wilcox, L. N.; Göltl, F.; Albarracin-Caballero, J. D.; Shih, A. J.; Ribeiro, F. H.; Gounder, R.; Schneider, W. F. Consequences of exchange-site heterogeneity and dynamics on the UV-visible spectrum of Cu-exchanged SSZ-13. *Chem. Sci.* **2019**, *10*, 2373−2384.
(72) Gillespie, D. T. A General Method for Numerically Simulation the Stochastic Time Evolution of Coupled Chemical Reactions. *J. Comput. Phys.* **1976**, *22*, 403−434.
(73) Gillespie, D. T. Approximate accelerated stochastic simulation of chemically reacting systems. *J. Chem. Phys.* **2001**, *115*, 1716−1733.
(74) Goodman, B. R.; Hass, K. C.; Schneider, W. F.; Adams, J. B. Statistical analysis of Al distributions and metal ion pairing probabilities in zeolites. *Catal. Lett.* **2000**, *68*, 85−93.
(75) Bates, S. A.; Verma, A. A.; Paolucci, C.; Parekh, A. A.; Anggara, T.; Yezerets, A.; Schneider, W. F.; Miller, J. T.; Delgass, W. N.; Ribeiro, F. H. Identification of the active Cu site in standard selective catalytic reduction with ammonia on Cu-SSZ-13. *J. Catal.* **2014**, *312*, 87−97.
(76) Di Iorio, J. R.; Nimlos, C. T.; Gounder, R. Introducing catalytic diversity into single-site chabazite zeolites of fixed composition via synthetic control of active site proximity. *ACS Catal.* **2017**, *7*, 6663−6674.
(77) Xiao, P.; Wang, Y.; Lu, Y.; De Baerdemaeker, T.; Parvulescu, A.-N.; Müller, U.; De Vos, D.; Meng, X.; Xiao, F.-S.; Zhang, W.; Marler, B.; Kolb, U.; Gies, H.; Yokoi, T. Effects of Al distribution in the Cu-exchanged AEI zeolites on the reaction performance of continuous direct conversion of methane to methanol. *Appl. Catal., B* **2023**, *325*, 122395.
(78) Deimund, M. A.; Harrison, L.; Lunn, J. D.; Liu, Y.; Malek, A.; Shayib, R.; Davis, M. E. Effect of Heteroatom Concentration in SSZ-13 on the Methanol-to-Olefins Reaction. *ACS Catal.* **2016**, *6*, 542−550.
(79) Liu, R.; Fan, B.; Zhang, W.; Wang, L.; Qi, L.; Wang, Y.; Xu, S.; Yu, Z.; Wei, Y.; Liu, Z. Increasing the Number of Aluminum Atoms in T3 Sites of a Mordenite Zeolite by Low-Pressure SiCl4 Treatment to Catalyze Dimethyl Ether Carbonylation. *Angew. Chem., Int. Ed.* **2022**, *134*, No. e202116990.
(80) Bae, J.; Dusselier, M. Synthesis strategies to control the Al distribution in zeolites: thermodynamic and kinetic aspects. *Chem. Commun.* **2023**, *59*, 852−867.
(81) Loewenstein, W. The distribution of aluminum in the tetrahedra of silicates and aluminates Walter Loewenstein. *Am. Mineral.* **1954**, *39*, 92−96.
(82) Chen, H.; Matsuoka, M.; Zhang, J.; Anpo, M. The reduction behavior of the Cu ion species exchanged into Y zeolite during the thermovacuum treatment. *J. Catal.* **2004**, *228*, 75−79.
(83) Vanelderen, P.; Vancauwenbergh, J.; Tsai, M. L.; Hadt, R. G.; Solomon, E. I.; Schoonheydt, R. A.; Sels, B. F. Spectroscopy and Redox Chemistry of Copper in Mordenite. *ChemPhysChem* **2014**, *15*, 91−99.
(84) Markovits, M. A.; Jentys, A.; Tromp, M.; Sanchez-Sanchez, M.; Lercher, J. A. Effect of Location and Distribution of Al Sites in ZSM-5 on the Formation of Cu-Oxo Clusters Active for Direct Conversion of Methane to Methanol. *Top. Catal.* **2016**, *59*, 1554−1563.
(85) Woertink, J. S.; Smeets, P. J.; Groothaert, M. H.; Vance, M. A.; Sels, B. F.; Schoonheydt, R. A.; Solomon, E. I. A [Cu2O]2+ core in Cu-ZSM-5, the active site in the oxidation of methane to methanol. *Proc. Natl. Acad. Sci. U.S.A.* **2009**, *106*, 18908−18913.
(86) Pankin, I. A.; Martini, A.; Lomachenko, K. A.; Soldatov, A. V.; Bordiga, S.; Borfecchia, E. Identifying Cu-oxo species in Cu-zeolites by XAS: A theoretical survey by DFT-assisted XANES simulation and EXAFS wavelet transform. *Catal. Today* **2020**, *345*, 125−135. Eighth Czech-Italian-Spanish Symposium on Zeolites and Catalysis
(87) Database of Zeolite Structures. http://www.iza-structure.org/databasesweb/(accessed on May 20, 2023).
(88) Park, M. B.; Park, E. D.; Ahn, W.-S. Recent Progress in Direct Conversion of Methane to Methanol Over Copper-Exchanged Zeolites. *Front. Chem.* **2019**, *7*, 514.
(89) Borfecchia, E.; Pappas, D. K.; Dyballa, M.; Lomachenko, K. A.; Negri, C.; Signorile, M.; Berlier, G. Evolution of active sites during selective oxidation of methane to methanol over Cu-CHA and Cu-MOR zeolites as monitored by operando XAS. *Catal. Today* **2019**, *333*, 17−27.
(90) Sun, L.; Wang, Y.; Wang, C.; Xie, Z.; Guan, N.; Li, L. Water-involved methane-selective catalytic oxidation by dioxygen over copper zeolites. *Chem* **2021**, *7*, 1557−1568.
(91) Molokova, A. Y.; Borfecchia, E.; Martini, A.; Pankin, I. A.; Atzori, C.; Mathon, O.; Bordiga, S.; Wen, F.; Vennestrøm, P. N. R.; Berlier, G.; Janssens, T. V. W.; Lomachenko, K. A. SO_2 Poisoning of Cu-CHA deNO_x Catalyst: The Most Vulnerable Cu Species Identified by X-ray Absorption Spectroscopy. *JACS Au* **2022**, *2*, 787−792.
(92) Knorpp, A. J.; Pinar, A. B.; Baerlocher, C.; McCusker, L. B.; Casati, N.; Newton, M. A.; Checchia, S.; Meyet, J.; Palagin, D.; van Bokhoven, J. A. Paired Copper Monomers in Zeolite Omega: The Active Site for Methane-to-Methanol Conversion. *Angew. Chem., Int. Ed.* **2021**, *60*, 5854−5858.
(93) Zhang, H.; Lv, J.; Zhang, Z.; Du, C.; Wang, S.; Lin, J.; Wan, S.; Wang, Y.; Xiong, H. Oxidation of Methane to Methanol by Water Over Cu/SSZ-13: Impact of Cu Loading and Formation of Active Sites. *ChemCatChem* **2022**, *14*, No. e202101609.
(94) Smeets, P. J.; Hadt, R. G.; Woertink, J. S.; Vanelderen, P.; Schoonheydt, R. A.; Sels, B. F.; Solomon, E. I. Oxygen precursor to the reactive intermediate in methanol synthesis by Cu-ZSM-5. *J. Am. Chem. Soc.* **2010**, *132*, 14736−14738.
(95) Bregante, D. T.; Wilcox, L. N.; Liu, C.; Paolucci, C.; Gounder, R.; Flaherty, D. W. Dioxygen Activation Kinetics over Distinct Cu Site Types in Cu-Chabazite Zeolites. *ACS Catal.* **2021**, *11*, 11873−11884.
(96) Sushkevich, V. L.; Smirnov, A. V.; van Bokhoven, J. A. Autoreduction of Copper in Zeolites: Role of Topology, Si/Al Ratio, and Copper Loading. *J. Phys. Chem. C* **2019**, *123*, 9926−9934.
(97) Di Iorio, J. R.; Gounder, R. Controlling the Isolation and Pairing of Aluminum in Chabazite Zeolites Using Mixtures of Organic and Inorganic Structure-Directing Agents. *Chem. Mater.* **2016**, *28*, 2236−2247.
(98) Schmidt, J. E.; Oord, R.; Guo, W.; Poplawsky, J. D.; Weckhuysen, B. M. Nanoscale tomography reveals the deactivation of automotive copper-exchanged zeolite catalysts. *Nat. Commun.* **2017**, *8*, 1666.
(99) Alberti, A. Location of Brønsted sites in mordenite. *Zeolites* **1997**, *19*, 411−415.
(100) Dědeček, J.; Sobalík, Z.; Wichterlová, B. Siting and Distribution of Framework Aluminium Atoms in Silicon-Rich Zeolites and Impact on Catalysis. *Catal. Rev.: Sci. Eng.* **2012**, *54*, 135−223.
(101) Jeffroy, M.; Nieto-Draghi, C.; Boutin, A. New Molecular Simulation Method To Determine Both Aluminum and Cation Location in Cationic Zeolites. *Chem. Mater.* **2017**, *29*, 513−523.
(102) Vanelderen, P.; Snyder, B. E. R.; Tsai, M.-L.; Hadt, R. G.; Vancauwenbergh, J.; Coussens, O.; Schoonheydt, R. A.; Sels, B. F.; Solomon, E. I. Spectroscopic Definition of the Copper Active Sites in Mordenite: Selective Methane Oxidation. *J. Am. Chem. Soc.* **2015**, *137*, 6383−6392.
(103) Jensen, Z.; Kwon, S.; Schwalbe-Koda, D.; Paris, C.; Gómez-Bombarelli, R.; Román-Leshkov, Y.; Corma, A.; Moliner, M.; Olivetti, E. A. Discovering Relationships between OSDAs and Zeolites through Data Mining and Generative Neural Networks. *ACS Cent. Sci.* **2021**, *7*, 858−867.
(104) Schwalbe-Koda, D.; Santiago-Reyes, O. A.; Corma, A.; Román-Leshkov, Y.; Moliner, M.; Gómez-Bombarelli, R. Repurposing Templates for Zeolite Synthesis from Simulations and Data Mining. *Chem. Mater.* **2022**, *34*, 5366−5376.
(105) Liu, R.; Fan, B.; Zhi, Y.; Liu, C.; Xu, S.; Yu, Z.; Liu, Z. Dynamic Evolution of Aluminum Coordination Environments in Mordenite Zeolite and Their Role in the Dimethyl Ether (DME) Carbonylation Reaction. *Angew. Chem., Int. Ed.* **2022**, *61*, No. e202210658.

https://doi.org/10.1021/jacsau.3c00632
JACS Au 2024, 4, 197−215

(106) Vjunov, A.; Fulton, J. L.; Huthwelker, T.; Pin, S.; Mei, D.; Schenter, G. K.; Govind, N.; Camaioni, D. M.; Hu, J. Z.; Lercher, J. A. Quantitatively Probing the Al Distribution in Zeolites. *J. Am. Chem. Soc.* **2014**, *136*, 8296−8306.
(107) Takaishi, T.; Kato, M.; Itabashi, K. Determination of the ordered distribution of aluminum atoms in a zeolitic framework. Part II. *Zeolites* **1995**, *15*, 21−32.
(108) Takaishi, T.; Kato, M.; Itabashi, K. Stability of the Al-O-Si-O-Al Linkage in a Zeolitic Framework. *J. Phys. Chem.* **1994**, *98*, 5742−5743.
(109) Dedecek, J.; Lucero, M. J.; Li, C.; Gao, F.; Klein, P.; Urbanova, M.; Tvaruzkova, Z.; Sazama, P.; Sklenak, S. Complex Analysis of the Aluminum Siting in the Framework of Silicon-Rich Zeolites. A Case Study on Ferrierites. *J. Phys. Chem. C* **2011**, *115*, 11056−11064.
(110) Dědeček, J.; Sklenak, S.; Li, C.; Wichterlová, B.; Gábová, V.; Brus, J.; Sierka, M.; Sauer, J. Effect of Al-Si-Al and Al-Si-Si-Al Pairs in the ZSM-5 Zeolite Framework on the 27Al NMR Spectra. A Combined High-Resolution 27Al NMR and DFT/MM Study. *J. Phys. Chem. C* **2009**, *113*, 1447−1458.
(111) Mafra, L.; Vidal-Moya, J. A.; Blasco, T. In *Annual Reports on NMR Spectroscopy*; Webb, G. A., Ed.; Academic Press, 2012; Vol. *77*, pp 259−351.
(112) Gray, A. E. Factors Determining the Distribution of Acid Sites in Zeolites. Ph.D. Thesis; University College London, 2016.
(113) Bodart, P.; Nagy, J. B.; Debras, G.; Gabelica, Z.; Jacobs, P. A. Aluminum siting in mordenite and dealumination mechanism. *J. Phys. Chem.* **1986**, *90*, 5183−5190.
(114) Zhao, Z. J.; Kulkarni, A.; Vilella, L.; Nørskov, J. K.; Studt, F. Theoretical Insights into the Selective Oxidation of Methane to Methanol in Copper-Exchanged Mordenite. *ACS Catal.* **2016**, *6*, 3760−3766.
(115) Vjunov, A.; Fulton, J. L.; Huthwelker, T.; Pin, S.; Mei, D.; Schenter, G. K.; Govind, N.; Camaioni, D. M.; Hu, J. Z.; Lercher, J. A. Correction to "Quantitatively Probing the Al Distribution in Zeolites. *J. Am. Chem. Soc.* **2015**, *137*, 2409−2409.
(116) Mahyuddin, M. H.; Staykov, A.; Shiota, Y.; Miyanishi, M.; Yoshizawa, K. Roles of Zeolite Confinement and Cu-O-Cu Angle on the Direct Conversion of Methane to Methanol by [Cu2(μ-O)]2+-Exchanged AEI, CHA, AFX, and MFI Zeolites. *ACS Catal.* **2017**, *7*, 3741−3751.
(117) Rhoda, H. M.; Plessers, D.; Heyer, A. J.; Bols, M. L.; Schoonheydt, R. A.; Sels, B. F.; Solomon, E. I. Spectroscopic Definition of a Highly Reactive Site in Cu-CHA for Selective Methane Oxidation: Tuning a Mono-μ-Oxo Dicopper(II) Active Site for Reactivity. *J. Am. Chem. Soc.* **2021**, *143*, 7531−7540.
(118) Guo, J., Sours, T., Holton, S., Sun, C., Kulkarni, A. R. Quantifying the Limits of Methane Activation in Cu-exchanged Zeolites using Reactive and Interpretable Machine Learning based Potentials. **2023**, Chemrxiv 10.26434/chemrxiv-2023-kwh3f.
(119) Artiglia, L.; Sushkevich, V. L.; Palagin, D.; Knorpp, A. J.; Roy, K.; van Bokhoven, J. A. In Situ X-ray Photoelectron Spectroscopy Detects Multiple Active Sites Involved in the Selective Anaerobic Oxidation of Methane in Copper-Exchanged Zeolites. *ACS Catal.* **2019**, *9*, 6728−6737.
(120) Plessers, D.; Heyer, A. J.; Rhoda, H. M.; Bols, M. L.; Solomon, E. I.; Schoonheydt, R. A.; Sels, B. F. Tuning Copper Active Site Composition in Cu-MOR through Co-Cation Modification for Methane Activation. *ACS Catal.* **2023**, *13*, 1906−1915.
(121) Ipek, B.; Lobo, R. F. Catalytic conversion of methane to methanol on Cu-SSZ-13 using N2O as oxidant. *Chem. Commun.* **2016**, *52*, 13401−13404.
(122) Kim, Y.; Kim, T. Y.; Lee, H.; Yi, J. Distinct activation of Cu-MOR for direct oxidation of methane to methanol. *Chem. Commun.* **2017**, *53*, 4116−4119.
(123) Zheng, J.; Lee, I.; Khramenkova, E.; Wang, M.; Peng, B.; Gutiérrez, O. Y.; Fulton, J. L.; Camaioni, D. M.; Khare, R.; Jentys, A.; Haller, G. L.; Pidko, E. A.; Sanchez-Sanchez, M.; Lercher, J. A. Importance of Methane Chemical Potential for Its Conversion to Methanol on Cu-Exchanged Mordenite. *Chemistry* **2020**, *26*, 7563−7567.
(124) Le, H. V.; Ho, P. H.; Trunschke, A.; Schomäcker, R.; Thomas, A. Stepwise conversion of methane to methanol on Cu and Fe/zeolites prepared in solid state: the effect of zeolite type and activation temperature. *J. Chem. Technol. Biotechnol.* **2023**, *98*, 2716−2725.
(125) Sushkevich, V. L.; Palagin, D.; van Bokhoven, J. A. The Effect of the Active-Site Structure on the Activity of Copper Mordenite in the Aerobic and Anaerobic Conversion of Methane into Methanol. *Angew. Chem.* **2018**, *130*, 9044−9048.
(126) Kvande, K.; Prodinger, S.; Schlimpen, F.; Beato, P.; Pale, P.; Chassaing, S.; Svelle, S. Copper-zeolites Prepared by Solid-state Ion Exchange - Characterization and Evaluation for the Direct Conversion of Methane to Methanol. *Top. Catal.* **2023**, *66*, 1406−1417.
(127) Le, H. V.; Parishan, S.; Sagaltchik, A.; Göbel, C.; Schlesiger, C.; Malzer, W.; Trunschke, A.; Schomäcker, R.; Thomas, A. Solid-State Ion-Exchanged Cu/Mordenite Catalysts for the Direct Conversion of Methane to Methanol. *ACS Catal.* **2017**, *7*, 1403−1412.
(128) Bozbag, S. E.; Alayon, E. M. C.; Pecháček, J.; Nachtegaal, M.; Ranocchiari, M.; van Bokhoven, J. A. Methane to methanol over copper mordenite: Yield improvement through multiple cycles and different synthesis techniques. *Catal.: Sci. Technol.* **2016**, *6*, 5011−5022.
(129) Smeets, P. J.; Groothaert, M. H.; Schoonheydt, R. A. Cu based zeolites: A UV-vis study of the active site in the selective methane oxidation at low temperatures. *Catal. Today* **2005**, *110*, 303−309.
(130) Artsiusheuski, M. A.; van Bokhoven, J. A.; Sushkevich, V. L. Structure of Selective and Nonselective Dicopper (II) Sites in CuMFI for Methane Oxidation to Methanol. *ACS Catal.* **2022**, *12*, 15626−15637.
(131) Tao, L.; Lee, I.; Sanchez-Sanchez, M. Cu oxo nanoclusters for direct oxidation of methane to methanol: formation, structure and catalytic performance. *Catal. Sci. Technol.* **2020**, *10*, 7124−7141.
(132) Pappas, D. K.; Borfecchia, E.; Dyballa, M.; Lomachenko, K. A.; Martini, A.; Berlier, G.; Arstad, B.; Lamberti, C.; Bordiga, S.; Olsbye, U.; Svelle, S.; Beato, P. Understanding and Optimizing the Performance of Cu-FER for The Direct CH4 to CH3OH Conversion. *ChemCatChem* **2019**, *11*, 621−627.
(133) Evans, J. D.; Coudert, F.-X. Predicting the Mechanical Properties of Zeolite Frameworks by Machine Learning. *Chem. Mater.* **2017**, *29*, 7833−7839.
(134) Kim, N.; Min, K. Optimal machine learning feature selection for assessing the mechanical properties of a zeolite framework. *Phys. Chem. Chem. Phys.* **2022**, *24*, 27031−27037.
(135) Colón, Y. J.; Snurr, R. Q. High-throughput computational screening of metal−organic frameworks. *Chem. Soc. Rev.* **2014**, *43*, 5735−5749.
(136) Knio, O.; Medford, A. J.; Nair, S.; Sholl, D. S. Database of Computation-Ready 2D Zeolitic Slabs. *Chem. Mater.* **2019**, *31*, 353−364.
(137) Schwalbe-Koda, D.; Kwon, S.; Paris, C.; Bello-Jurado, E.; Jensen, Z.; Olivetti, E.; Willhammar, T.; Corma, A.; Román-Leshkov, Y.; Moliner, M.; Gómez-Bombarelli, R. A priori control of zeolite phase competition and intergrowth with high-throughput simulations. *Science* **2021**, *374*, 308−315.
(138) Daya, R.; Joshi, S. Y.; Luo, J.; Dadi, R. K.; Currier, N. W.; Yezerets, A. On kinetic modeling of change in active sites upon hydrothermal aging of Cu-SSZ-13. *Appl. Catal., B* **2020**, *263*, 118368.
(139) Deka, D. J.; Daya, R.; Ladshaw, A.; Trandal, D.; Joshi, S. Y.; Partridge, W. P. Assessing impact of real-world aging on Cu-redox half cycles of a Cu-SSZ-13 SCR catalyst via transient response measurements and kinetic modeling. *Appl. Catal., B* **2022**, *309*, 121233.
(140) Kwak, J. H.; Tran, D.; Burton, S. D.; Szanyi, J.; Lee, J. H.; Peden, C. H. Effects of hydrothermal aging on NH3-SCR reaction over Cu/zeolites. *J. Catal.* **2012**, *287*, 203−209.
(141) Albarracin-Caballero, J. D.; Khurana, I.; Di Iorio, J. R.; Shih, A. J.; Schmidt, J. E.; Dusselier, M.; Davis, M. E.; Yezerets, A.; Miller, J.

https://doi.org/10.1021/jacsau.3c00632
JACS Au 2024, 4, 197−215

T.; Ribeiro, F. H.; Gounder, R. Structural and kinetic changes to small-pore Cu-zeolites after hydrothermal aging treatments and selective catalytic reduction of NOx with ammonia. *React. Chem. Eng.* **2017**, *2*, 168−179.
(142) Jin, M.; Ravi, M.; Lei, C.; Heard, C. J.; Brivio, F.; Tošner, Z.; Grajciar, L.; van Bokhoven, J. A.; Nachtigall, P. Dynamical Equilibrium between Brønsted and Lewis Sites in Zeolites: Framework-Associated Octahedral Aluminum. *Angew. Chem., Int. Ed.* **2023**, *135*, No. e202306183.
(143) Khramenkova, E. V.; Venkatraman, H.; Soethout, V.; Pidko, E. A. Global optimization of extraframework ensembles in zeolites: structural analysis of extraframework aluminum species in MOR and MFI zeolites. *Phys. Chem. Chem. Phys.* **2022**, *24*, 27047−27054.
(144) Lee, I.; Lee, M. S.; Tao, L.; Ikuno, T.; Khare, R.; Jentys, A.; Huthwelker, T.; Borca, C. N.; Kalinko, A.; Gutiérrez, O. Y.; et al. Activity of Cu−Al−Oxo Extra-Framework Clusters for Selective Methane Oxidation on Cu-Exchanged Zeolites. *JACS Au* **2021**, *1*, 1412−1421.
(145) Khramenkova, E. V.; Medvedev, M. G.; Li, G.; Pidko, E. A. Unraveling the Nature of Extraframework Catalytic Ensembles in Zeolites: Flexibility and Dynamics of the Copper-Oxo Trimers in Mordenite. *J. Phys. Chem. Lett.* **2021**, *12*, 10906−10913.
(146) Pophale, R.; Cheeseman, P. A.; Deem, M. W. A database of new zeolite-like materials. *Phys. Chem. Chem. Phys.* **2011**, *13*, 12407−12412.
(147) Hagberg, A. A., Schult, D. A., Swart, P. J. Exploring network structure, dynamics, and function using NetworkX. *7th Python in Science Conference (SciPy)*, 2008; pp 11−15.
(148) Schwalbe-Koda, D.; Jensen, Z.; Olivetti, E.; Gómez-Bombarelli, R. Graph similarity drives zeolite diffusionless transformations and intergrowth. *Nat. Mater.* **2019**, *18*, 1177−1181.
(149) Momma, K.; Izumi, F. *VESTA3* for three-dimensional visualization of crystal, volumetric and morphology data. *J. Appl. Crystallogr.* **2011**, *44*, 1272−1276.
(150) Wales, D. J.; Doye, J. P. Global optimization by basin-hopping and the lowest energy structures of Lennard-Jones clusters containing up to 110 atoms. *J. Phys. Chem. A* **1997**, *101*, 5111−5116.
(151) Olson, B.; Hashmi, I.; Molloy, K.; Shehu, A. Basin Hopping as a General and Versatile Optimization Framework for the Characterization of Biological Macromolecules. *Adv. Artif. Intell.* **2012**, *2012*, 1−19.
(152) Virtanen, P.; Gommers, R.; Oliphant, T. E.; Haberland, M.; Reddy, T.; Cournapeau, D.; Burovski, E.; Peterson, P.; Weckesser, W.; Bright, J.; et al. SciPy 1.0: fundamental algorithms for scientific computing in Python. *Nat. Methods* **2020**, *17*, 261−272.
(153) Vandermause, J.; Torrisi, S. B.; Batzner, S.; Xie, Y.; Sun, L.; Kolpak, A. M.; Kozinsky, B. On-the-fly active learning of interpretable Bayesian force fields for atomistic rare events. *npj Comput. Mater.* **2020**, *6*, 20.
(154) Nystrom, S.; Hoffman, A.; Hibbitts, D. Tuning Brønsted Acid Strength by Altering Site Proximity in CHA Framework Zeolites. *ACS Catal.* **2018**, *8*, 7842−7860.
(155) Bruzzese, P. C.; Salvadori, E.; Civalleri, B.; Jäger, S.; Hartmann, M.; Pöppl, A.; Chiesa, M. The Structure of Monomeric Hydroxo-CuII Species in Cu-CHA. A Quantitative Assessment. *J. Am. Chem. Soc.* **2022**, *144*, 13079−13083.
(156) Kresse, G.; Furthmüller, J. Efficient iterative schemes for ab initio total-energy calculations using a plane-wave basis set. *Phys. Rev. B: Condens. Matter Mater. Phys.* **1996**, *54*, 11186.
(157) Blöchl, P. E. Projector augmented-wave method. *Phys. Rev. B: Condens. Matter Mater. Phys.* **1994**, *50*, 17953−17979.
(158) Perdew, J. P.; Burke, K.; Ernzerhof, M. Generalized Gradient Approximation Made Simple. *Phys. Rev. Lett.* **1996**, *77*, 3865−3868.
(159) Grimme, S.; Antony, J.; Ehrlich, S.; Krieg, H. A consistent and accurate ab initio parametrization of density functional dispersion correction (DFT-D) for the 94 elements H-Pu. *J. Chem. Phys.* **2010**, *132*, 154104.
(160) Grimme, S.; Ehrlich, S.; Goerigk, L. Effect of the damping function in dispersion corrected density functional theory. *J. Comput. Chem.* **2011**, *32*, 1456−1465.
(161) Chen, L.; Janssens, T. V. W.; Grönbeck, H. A comparative test of different density functionals for calculations of NH 3-SCR over Cu-Chabazite. *Phys. Chem. Chem. Phys.* **2019**, *21*, 10923−10930.
(162) Goncalves, T. J.; Plessow, P. N.; Studt, F. On the Accuracy of Density Functional Theory in Zeolite Catalysis. *ChemCatChem* **2019**, *11*, 4368−4376.
(163) Solomon, E. I.; Heppner, D. E.; Johnston, E. M.; Ginsbach, J. W.; Cirera, J.; Qayyum, M.; Kieber-Emmons, M. T.; Kjaergaard, C. H.; Hadt, R. G.; Tian, L. Copper Active Sites in Biology. *Chem. Rev.* **2014**, *114*, 3659−3853.
(164) Li, Y. P.; Gomes, J.; Mallikarjun Sharada, S.; Bell, A. T.; Head-Gordon, M. Improved force-field parameters for QM/MM simulations of the energies of adsorption for molecules in zeolites and a free rotor correction to the rigid rotor harmonic oscillator model for adsorption enthalpies. *J. Phys. Chem. C* **2015**, *119*, 1840−1850.
(165) Chase, M. W. *NIST-JANAF Thermochemical Tables 2 Vol.-Set (Journal of Physical and Chemical Reference Data Monographs)*, 4th ed.; American Institute of Physics, 1998.
(166) Friedman, J. H. Greedy function approximation: A gradient boosting machine. *Ann. Stat.* **2001**, *29*, 1189−1232.
(167) Hjorth Larsen, A.; Jørgen Mortensen, J.; Blomqvist, J.; Castelli, I. E.; Christensen, R.; Dułak, M.; Friis, J.; Groves, M. N.; Hammer, B.; Hargus, C.; et al. The atomic simulation environment—a Python library for working with atoms. *J. Phys.: Condens. Matter* **2017**, *29*, 273002.
(168) Chen, T.; Guestrin, C. *XGBoost: A Scalable Tree Boosting System*. KDD '16, San Francisco, CA, USA, 2016.
(169) Caruana, R., Niculescu-Mizil, A. An empirical comparison of supervised learning algorithms. *ACM International Conference Proceeding Series*, 2006; Vol. *148*, pp 161−168.
(170) Ducamp, M.; Coudert, F.-X. Prediction of Thermal Properties of Zeolites through Machine Learning. *J. Phys. Chem. C* **2022**, *126*, 1651−1660.
(171) Friedman, J. H.; Meulman, J. J. Multiple additive regression trees with application in epidemiology. *Stat. Med.* **2003**, *22*, 1365−1381.
(172) Elith, J.; Leathwick, J. R.; Hastie, T. A working guide to boosted regression trees. *J. Anim. Ecol.* **2008**, *77*, 802−813.

https://doi.org/10.1021/jacsau.3c00632
JACS Au 2024, 4, 197−215